Contribution of expanded marine sulfur chemistry to the seasonal variability of DMS oxidation products and size-resolved sulfate aerosol

Linia Tashmim[1], William C. Porter[1], Qianjie Chen[2], Becky Alexander[3], Charles H. Fite[4], Christopher D. Holmes[4], Jeffrey R. Pierce[5], Betty Croft[6], and Sakiko Ishino[7]

[1]Department of Environmental Sciences, University of California, Riverside, CA, USA
[2]Department of Civil and Environmental Engineering, The Hong Kong Polytechnic University, Hong Kong, China
[3]Department of Atmospheric Sciences, University of Washington, Seattle, WA, USA
[4]Department of Earth, Ocean and Atmospheric Science, Florida State University, Tallahassee, FL, USA
[5]Department of Atmospheric Science, Colorado State University, Fort Collins, CO, USA
[6]Department of Physics and Atmospheric Science, Dalhousie University, Halifax, Nova Scotia, Canada
[7]Institute of Nature and Environmental Technology, Kanazawa University, Japan

Correspondence: Linia Tashmim (ltash001@ucr.edu) and William C. Porter (william.porter@ucr.edu)

Abstract. Marine emissions of dimethyl sulfide (DMS) and the subsequent formation of its oxidation products methane sulfonic acid (MSA) and sulfuric acid (H_2SO_4) are well-known natural precursors of atmospheric aerosols, contributing to particle mass and cloud formation over ocean and coastal regions. Despite a long-recognized and well-studied role in the marine troposphere, DMS oxidation chemistry remains a work in progress within many current air quality and climate models, with recent advances exploring heterogeneous chemistry and uncovering previously unknown intermediate species. With the identification of additional DMS oxidation pathways and intermediate species influencing its eventual fate, it is important to understand the impact of these pathways on the overall sulfate aerosol budget and aerosol size distribution. In this work, we update and evaluate the DMS oxidation mechanism of the chemical transport model GEOS-Chem by implementing expanded DMS oxidation pathways into the model. These updates include gas- and aqueous-phase reactions, the formation of the intermediates dimethyl sulfoxide (DMSO) and methane sulphinic acid (MSIA), as well as cloud loss and aerosol uptake of the recently quantified intermediate hydroperoxymethyl thioformate (HPMTF). We find that this updated mechanism collectively decreases the global mean surface-layer gas-phase sulfur dioxide (SO_2) mixing ratio by 35% and enhances sulfate aerosol (SO_4^{2-}) mixing ratio by 22%. We further perform sensitivity analyses exploring the contribution of cloud loss and aerosol uptake of HPMTF to the overall sulfur budget. Comparing modeled concentrations to available observations we find improved biases relative to previous studies. To quantify impacts of these chemistry updates on global particle size distributions and mass concentration we use the TOMAS aerosol microphysics module coupled to GEOS-Chem, finding changes in particle formation and growth affect the size distribution of aerosol. With this new DMS-oxidation scheme the global annual mean surface layer number concentration of particles with diameters smaller than 80 nm decreases by 12.8%, with cloud loss processes related to HPMTF mostly responsible for this reduction. However, global annual mean number of particles larger than 80 nm increases by 3.1%, suggesting that the new scheme promotes seasonal particle growth to these sizes capable of acting as cloud condensation nuclei (CCN).

1 Introduction

Dimethyl sulfide (DMS: CH_3SCH_3) is the most abundant biological source of sulfate aerosol and has a significant influence on Earth's radiation budget and climate due to its contribution to atmospheric marine particle (Charlson et al., 1987; Fung et al., 2022). In the atmosphere, DMS reacts with hydroxyl radical (OH), nitrate radical (NO_3), ozone (O_3) and various halogen species (e.g., chlorine (Cl) and bromine oxide (BrO)), primarily forming sulfur dioxide (SO_2) and methyl sulfonic acid (MSA; CH_3SO_3H) (Chen et al., 2018; Faloona, 2009; Hoffmann et al., 2016). These oxidation products are considered key influences on the formation and evolution of natural aerosols and clouds along with their associated climate impacts, especially in the marine boundary layer (MBL) (Carslaw et al., 2013; Sipilä et al., 2010; Schobesberger et al., 2013; Thomas et al., 2010; von Glasow and Crutzen, 2004). SO_2 and MSA formed by DMS oxidation can be deposited on Earth surface or further oxidize affecting the size distribution of aerosol and cloud microphysics (Leaitch et al., 2013; Wollesen de Jonge et al., 2021). SO_2 can either oxidize in the gas-phase by reaction with the OH radical forming H_2SO_4, which can participate in nucleation and early growth of particles in the atmosphere, or it can be taken up by cloud droplets and undergo aqueous phase oxidation by reaction with H_2O_2, O_3 and O_2 catalyzed by transition metals (Mn, Fe) forming SO_4^{2-} and generally only contributing to the growth of aerosol particles (Hoyle et al., 2016; Kulmala, 2003; Alexander et al., 2009). The hypohalous acids (HOBr, HOCl, HOI) also plays significant role in aqueous-phase sulfate production in the marine boundary layer (MBL) (Chen et al., 2016; Sherwen et al., 2016b). Recent studies have highlighted the importance of natural aerosols originating from DMS oxidation and their contribution to the uncertainty of aerosol radiative forcing in climate models (Carslaw et al., 2013; Fung et al., 2022; Rosati et al., 2022; Novak et al., 2021, 2022). Since DMS-derived aerosol is a major source of uncertainty in estimating the global natural aerosol burden and associated aerosol indirect radiative forcing, a more accurate representation of DMS oxidation and particle formation processes is an important step towards improved Earth system and climate modeling.

Although the chemistry of DMS oxidation has been previously studied in great detail, known uncertainties and omissions in the current mechanism remain in current air quality and chemical transport models (Barnes et al., 2006; Fung et al., 2022; Hoffmann et al., 2016, 2021). Furthermore, while increasingly complex and experimentally validated mechanisms are under ongoing development, DMS oxidation processes in many current chemical transport models continue to be represented through simplified gas-phase reactions with the tropospheric oxidants OH and NO_3, producing the two major oxidation products SO_2 and MSA at a fixed ratio as shown in R1-R3 in Table 1 (Chen et al., 2018; Chin et al., 1996; Veres et al., 2020). This type of simplified mechanism neglects the formation and loss of important intermediates such as dimethyl sulfoxide (DMSO: CH_3SOCH_3), methane sulphinic acid (MSIA: CH_3SO_2H) and the recently discovered oxidation product hydroperoxymethyl thioformate (HPMTF: $HOOCH_2SCHO$) (Berndt et al., 2019; Veres et al., 2020; Wu et al., 2015; Khan et al., 2021).

These omissions can have major consequences on product yields of DMS oxidation, thereby affecting the aerosol burdens. For example, the OH-addition pathway of DMS forms DMSO and MSIA as the intermediates, which has been identified as a dominant source of MSA via their aqueous-phase oxidation, and a fraction of that MSA subsequently undergoes aqueous-phase oxidation to form sulfate aerosol (Chen et al., 2018; Ishino et al., 2021; Zhu et al., 2006; von Glasow and Crutzen, 2004). Previous studies suggest that BrO contributes to 8 – 30% of total DMS

88 loss, highlighting the importance of this pathway as well (Breider et al., 2010; Boucher et al., 2003;
89 Chen et al., 2018; Khan et al., 2016). More recent experimental and laboratory studies have
90 confirmed the formation of methylthiomethyl peroxy radicals (CH_3CH_2OO; abbreviated as MSP
91 or MTMP) from the H-abstraction channel of OH oxidation, which can subsequently lead to a
92 series of rapid intramolecular H-shift isomerization reactions, ultimately resulting in the formation
93 of the stable intermediate HPMTF (Berndt et al., 2019; Veres et al., 2020; Vermeuel et al., 2020;
94 Wu et al., 2015; Fung et al., 2022; Jernigan et al., 2022a). It has been reported that 30–46% of
95 emitted DMS forms HPMTF according to different modeling studies and this falls within the
96 observational range from NASA Atmospheric Tomography ATom-3 and ATom-4 flight
97 campaigns where about 30–40% DMS was oxidized to HPMTF along their flight tracks (Fung et
98 al., 2022; Veres et al., 2020; Novak et al., 2021). Subsequent investigation of the isomerization
99 rate and heterogeneous loss of HPMTF in cloud droplets and aerosol shows a high production rate
100 of marine carbonyl sulfide (OCS) from the chemical loss of HPMTF, a potential precursor of
101 stratospheric sulfate aerosol and significant inhibitor of cloud condensation nuclei (CCN)
102 formation due to the resulting reduction of surface SO_2 (Jernigan et al., 2022a). With the latest
103 experimental findings on heterogeneous loss process of HPMTF and experimentally validated
104 oxidation reactions for OCS formation directly from HPMTF it is necessary to include these
105 reactions as part of the DMS oxidation mechanism as these will have impact on overall yield of
106 SO_2, thus affecting the formation probability of CCN (Jernigan et al., 2022a, b).
107
108 **Table 1.** The three DMS oxidation reactions in the standard GEOS-Chem chemical mechanism

Reactions	Rate (s^{-1})	
DMS+ $OH_{(abstraction)}$ → SO_2 + CH_3O_2 + CH_2O	1.20e-11*exp(-280/T)	(R1)
DMS+ $OH_{(addition)}$ → 0.75 SO_2 + 0.25 MSA + CH_3O_2	$8.2\times10^{-39}[O_2]e^{5376/T}/(1+1.05\times10^{-5}([O2]/[M])e^{3644/T})$ $cm^3molecule^{-1}s^{-1}$	(R2)
DMS+ NO_3 → SO_2+ HNO_3+ CH_3O_2+ CH_2O	1.90e-13*exp(530/T)	(R3)

109
110 Considering these and other consequences of complex DMS oxidation processes, a heavily
111 simplified oxidation scheme will necessarily neglect potentially important reaction intermediates
112 along with their production and loss pathways, with implications for the concentration and
113 distribution of the oxidation products, including particulate sulfate. Differing intermediate
114 lifetimes further influence sulfur removal and transport depending on the relative dominance of
115 pathways. Thus, the exclusion of key pathways and intermediate species can lead to errors in the
116 representation of the spatial distribution of both gas- and particle-phase sulfur species, as well as
117 global sulfur burden.

118 The DMS oxidation products sulfate and MSA play an important role in Earth's radiative budget
119 through cloud droplet formation, and the extent of this role depends on how efficiently they can
120 produce and grow new particles in the marine atmosphere (Thomas et al., 2010). SO_2 can oxidize
121 in the gas-phase the forming H_2SO_4, which acts as a key product contributing to nucleation and
122 condensational growth as shown in Figure 1. SO_2 oxidizing through aqueous chemistry in cloud
123 droplets does contribute to particle growth rates by providing larger aerosol during cloud
124 evaporation that acts as more efficient CCN (Kaufman and Tanré, 1994). On the other hand, MSA
125 might participates in nucleation along with sulfuric acid in presence of amines or ammonia
126 (Johnson and Jen, 2023). Recent studies have highlighted the importance of aqueous-phase
127 chemistry in the formation and loss of MSA (Boniface et al., 2000; Chen et al., 2015; Kaufman
128 and Tanré, 1994; Kulmala et al., 2000).
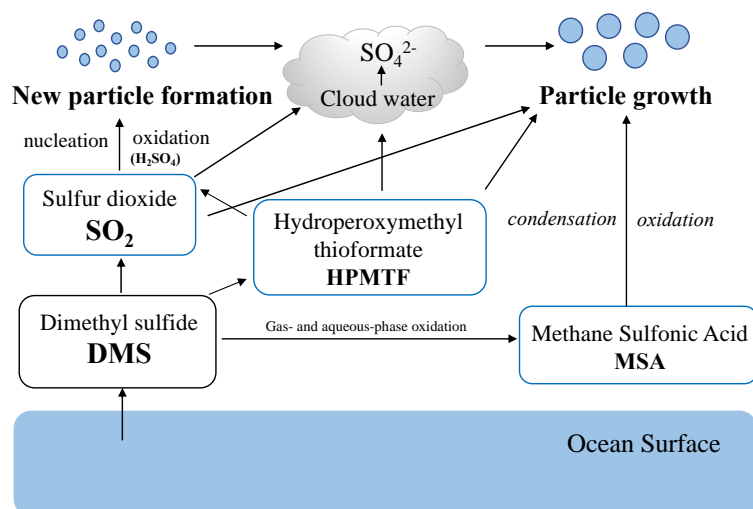
Figure 1 Modified DMS oxidation mechanism used in this work (simulation MOD) showing the formation of major stable oxidation products (blue-outline boxes) including newly identified intermediate HPMTF, and their contribution to new particle formation or growth of existing particles. Note that we include gas-phase and aqueous-phase chemistry of DMSO, MSIA and OCS in the mechanism, which counts towards their contribution to the formation of major oxidation products of DMS, but that these pathways are not explicitly shown here to maintain visual clarity.

129 Additionally, the recently identified intermediate HPMTF also has the potential for further gas-
130 phase oxidation. Under cloud-free conditions, HPMTF can undergo gas-phase oxidation by OH,
131 producing SO_2 and eventually leading to the formation of non-sea-salt-SO_4^{2-}. This sulfate can
132 contribute to aerosol formation and growth processes, with climate implications (Galí et al., 2019).
133 Other work has used direct airborne eddy covariance flux measurements to explain the chemical
134 fate of HPMTF in the MBL, finding that in cloudy conditions chemical loss due to aqueous phase
135 reactions in clouds is the major HPMTF removal process (Novak et al., 2021). In the same study,
136 global model simulations showed a 35% reduction in global annual average SO_2 production from
137 DMS and a 24% reduction in the near-surface (0 to 3 km) global annual average SO_2
138 concentrations over the ocean as a result of this process (Novak et al., 2021). Thus, a complete
139 representation of cloud loss and aerosol uptake is needed to effectively evaluate the atmospheric
140 impacts of marine DMS and their connections to cloud formation (Novak et al., 2021; Holmes et
141 al., 2019).

142 To better understand the marine sulfur budget, as well as the eventual formation, size distribution,
143 and seasonality of sulfate aerosol, we use the global chemical transport model GEOS-Chem,
144 integrating previously developed mechanisms along with newly proposed pathways involving the
145 formation and loss of the intermediates DMSO, MSIA, and HPMTF. As part of this work, we
146 further quantify the atmospheric impacts of individual reactions and mechanisms, evaluate
147 uncertainties in the chemical mechanism, and identify improvements necessary to better represent
148 the impacts of DMS more accurately on atmospheric chemistry and climate. The resulting
149 integrated scheme provides a more complete representation of marine sulfur and sulfate aerosol
150 species in marine tropospheric environments compared to the simplified base GEOS-Chem
151 mechanism, with improved comparisons to aircraft and surface observations. Since aerosols are a
152 major contributor to uncertainty in climate forcing, improving oxidation and aerosol formation
153 mechanisms by adding and optimizing neglected reactions in models is a crucial step towards a
154 more mechanistically robust representation of particle yields and sensitivities. We further perform

155   multiple sensitivity tests to investigate how the uncertainty in heterogeneous uptake of the newly
156   identified HPMTF could influence DMS chemistry and tropospheric aerosol formation (Holmes
157   et al., 2019; Novak et al., 2021). In a broader sense our work provides a more detailed story on the
158   heterogeneous loss, fate, and ultimate impacts of DMS and its oxidation products, improving our
159   understanding of a key ocean-atmosphere interaction in the context of global change.

2   Methodology

To simulate DMS chemistry and its oxidation products GEOS-Chem global chemical transport model v12.9.3 is used. Impacts on simulated aerosol size, number and mass concentration are considered by coupling the TwO-Moment Aerosol Sectional (TOMAS) aerosol microphysics module with GEOS-Chem v12.9.3 (GC-TOMAS) (https://github.com/geoschem/geos-chem/tree/12.9.3) (Adams and Seinfeld, 2002; Kodros and Pierce, 2017). The default GEOS-Chem chemical mechanism contains detailed HO_x–NO_x–VOC–O_3–halogen tropospheric chemistry along with recently updated halogen chemistry and in-cloud processing (Bey et al., 2001; Holmes et al., 2019; Chen et al., 2017; Parrella et al., 2012; Schmidt et al., 2016; Wang et al., 2019). The DMS emission flux from ocean are controlled by a gas transfer velocity which is dependent on sea surface temperature and wind speed (Johnson, 2010) and a climatology of concentrations in seawater (Lana et al., 2011; Nightingale et al., 2000). The aqueous-phase concentration of O_3 in aerosols or cloud droplets is calculated assuming gas-liquid equilibrium and aqueous-phase concentration of OH is calculated following $[OH_{(aq)}] = \delta[OH_{(g)}]$ where, $\delta = 1 \times 10^{-19}$ M cm^3 molecule^{-1} (Jacob et al., 2005; Chen et al., 2018).

In this study, TOMAS tracks aerosol number and the mass of each aerosol species in 15 logarithmically sized bins, with sizes in this analysis ranging from 3 nm to 10 µm (Lee and Adams, 2012; Lee et al., 2013). All binned aerosol species undergo interactive microphysics, allowing the calculation of aerosol number budgets (Westervelt et al., 2013). The version of GC-TOMAS used here includes 47 vertical levels, a horizontal resolution of $4º \times 5º$, and the GEOS-FP data product for meteorological inputs. Simulations are performed for 2018, with 11 months of discarded model spin up. Nucleation is simulated via a ternary nucleation scheme involving water, sulfuric acid, and ammonia with nucleation rates scaled by 10^{-5} (Napari et al., 2002; Westervelt et al., 2013). In low-ammonia regions (less than 1 pptv), a binary nucleation scheme involving water and sulfuric acid is instead used (Vehkamäki et al., 2002). Previously GC-TOMAS has been used for aerosol simulations to investigate topics such as the aerosol cloud-albedo effect and cloud condensation nuclei formation (Kodros et al., 2016; Kodros and Pierce, 2017; Pierce and Adams, 2006; Westervelt et al., 2013). Aerosol species available for GC-TOMAS simulations are sulfate, aerosol water, black carbon, organic carbon, mineral dust, and sea salt (Alexander et al., 2005; Bey et al., 2001; Duncan Fairlie et al., 2007; Pye et al., 2009). The wet and dry deposition scheme for aerosols and gas species are based on previous studies (Amos et al., 2012; Emerson et al., 2020; Liu et al., 2001; Wesely, 1989; Wang et al., 1998).

We refer to simulations performed using only these three DMS oxidation reactions (Table 1) as the "BASE", involving only the direct formation of SO_2 and MSA in gas-phase (Chin et al., 1996). We further implement and evaluate a custom chemical mechanism for DMS oxidation, referred to as "MOD" (Table 2-4), representing an integration of three individual DMS oxidation mechanism updates explored previously using GEOS-Chem and CAM6-Chem, along with HPMTF loss via heterogenous chemistry in clouds and aerosols and dry and wet deposition of HPMTF (Chen et al., 2018; Fung et al., 2022; Veres et al., 2020; Novak et al., 2021). Loss of HPMTF in clouds follow entrainment-limited uptake which used a chemical rate expression to control rate of mixing between cloudy and clear air (Holmes et al., 2019). In GC-TOMAS we use specific subroutine that take amount of sulfate produced via in-cloud oxidation and condense it into an existing aerosol size distribution. So, mass of sulfate produced by oxidation is portioned to the various size bins according to the number of particles in that size bin. TOMAS microphysics accounts for H_2SO_4

formation based on gas-phase oxidation of SO_2 included in the kinetic preprocessor (KPP) equation list valid for the simulation BASE. Since there are additional sources of sulfate in the integrated DMS oxidation mechanism both in gas and aqueous phase, we made necessary changes in the KPP code to explicitly track H_2SO_4 formation by gas phase oxidation of SO_2. On the other hand, code changes for sulfate formed by heterogeneous oxidation of MSA and HPMTF (in clouds and aerosols) were added in the GEOS-Chem microphysics module that also handles in-cloud oxidation of SO_2 in GC version 12.9.3 (Park et al., 2004; Trivitayanurak et al., 2008).

Table 2. Overview of the DMS oxidation mechanism via OH-addition pathway.

Gas-phase reactions	Rate (s^{-1})	References
DMS + OH → 0.60SO$_2$ + 0.4DMSO + CH$_3$O$_2$	$8.2\times10^{-39}[O_2]e^{5376/T}/(1+1.05\times10^{-5}([O2]/[M])e^{3644/T})$ cm^{3}molecule^{-1}s^{-1}	(Burkholder et al., 2015; Pham et al., 1995; Spracklen et al., 2005)
DMS + BrO → DMSO + Br	1.50e-14*exp(1000/T)	(Bräuer et al., 2013; Hoffmann et al., 2016)
DMS + O$_3$ → SO$_2$	1.50e-19	(Burkholder et al., 2015; Du et al., 2007)
DMSO + OH → 0.95MSIA + 0.05SO$_2$	6.10e-12*exp(800/T)	(Burkholder et al., 2015; von Glasow and Crutzen, 2004)
MSIA + OH → 0.9SO$_2$ + 0.1MSA	9.00e-11	(Burkholder et al., 2015)
MSIA + O$_3$ → MSA	2.00e-18	(von Glasow and Crutzen, 2004; Lucas and Prinn, 2002)

Aqueous-phase reactions	k$_{298}$ [M^{-1}s^{-1}]	References
DMS (aq) + O$_3$ (aq) → DMSO (aq) + O$_2$ (aq)	8.61×10^8	(Gershenzon et al., 2001; Hoffmann et al., 2016)
DMSO (aq) + OH (aq) → MSIA (aq)	6.65×10^9	(Zhu et al., 2003; Hoffmann et al., 2016)
MSIA (aq) + OH (aq) → MSA (aq)	6.00×10^9	(Sehested and Holcman, 1996; Hoffmann et al., 2016)
MSI$^-$ (aq) + OH (aq) → MSA (aq)	1.20×10^{10}	(Bardouki et al., 2002; Hoffmann et al., 2016)
MSIA (aq) + O$_3$ (aq) → MSA (aq)	3.50×10^7	(Hoffmann et al., 2016)
MSI$^-$ (aq) + O$_3$ (aq) → MSA (aq)	2.00×10^6	(Flyunt et al., 2001; Hoffmann et al., 2016)
MSA (aq) + OH (aq) → SO$_4^{2-}$	1.50×10^7	(Hoffmann et al., 2016)
MS$^-$ (aq) + OH (aq) → SO$_4^{2-}$ (aq)	1.29×10^7	(Zhu et al., 2003; Hoffmann et al., 2016)

Table 3. Overview of the DMS oxidation mechanism involving HPMTF formation.

Gas-phase reactions	Rate (s^{-1})	References
MSP (CH$_3$SCH$_2$OO) → OOCH$_2$SCH$_2$OOH	2.2433e11*exp(-9.8016e3/T)*(1.0348e8/T^3)	(Berndt et al., 2019; Veres et al., 2020; Wollesen de Jonge et al., 2021)
OOCH$_2$SCH$_2$OOH → HPMTF (HOOCH$_2$SCHO) + OH	6.0970e11*exp(-9.489e3/T)*(1.1028e8/T^3)	(Berndt et al., 2019; Veres et al., 2020; Wollesen de Jonge et al., 2021)
OOCH$_2$SCH$_2$OOH + NO → HOOCH$_2$S + NO$_2$ + HCHO	4.9e-12*exp(260/T)	(Saunders et al., 2003)
MSP + HO$_2$ → CH$_3$SCH$_2$OOH + O$_2$	1.13e-13*exp(1300/T)	MCMv3.3.1, (Wollesen de Jonge et al., 2021)
CH$_3$SCH$_2$OOH + hv → CH$_3$SCH$_2$O +OH	J(41)	MCMv3.3.1, (Wollesen de Jonge et al., 2021)
HPMTF + OH→ HOOCH$_2$SCO + H$_2$O	4.00e-12	(Jernigan et al., 2022a)

HPMTF + OH→ 0.13OCS + 0.87SO$_2$ + CO	1.40e-11	(Jernigan et al., 2022a)
OCS + OH → SO$_2$	1.13e-13*exp(1200/T)	(Jernigan et al., 2022a)
HOOCH$_2$SCO → HOOCH$_2$S + CO	9.2e9*exp(-505.4/T)	(Wu et al., 2015)
HOOCH$_2$SCO → OH + CH$_2$O + OCS	1.6e7*exp(-1468.6/T)	(Wu et al., 2015)
HOOCH$_2$S + O$_3$ → HOOCH$_2$SO + O$_2$	1.15e-12*exp(430/T)	(Saunders et al., 2003)
HOOCH$_2$S + NO$_2$ → HOOCH$_2$SO + NO	6.0e-11*exp(240/T)	(Saunders et al., 2003)
HOOCH$_2$SO + O$_3$ → SO$_2$ + CH$_2$O + OH + O$_2$	4.0e-13	(Saunders et al., 2003)
HOOCH$_2$SO + NO$_2$ → SO$_2$ + CH$_2$O + OH + NO	1.2e-11	(Saunders et al., 2003)

215
216 **Table 4.** Overview of the MSA-producing branch of the H-abstraction pathway of DMS oxidation.

Gas-phase reactions	Rate (s^{-1})	Original References
DMS + OH → MSP (CH$_3$SCH$_2$OO) + H$_2$O	1.12e-11*exp(-250/T)	(Saunders et al., 2003)
DMS + Cl → 0.45MSP + 0.55C$_2$H$_6$SCl + 0.45HCl	3.60e-10	(Fung et al., 2022; Enami et al., 2004)
C$_2$H$_6$SCl → DMSO + ClO	4.00e-18	(Hoffmann et al., 2016)
DMS + NO$_3$ → MSP + HNO$_3$	1.9e-13*exp(520/T)	(Novak et al., 2021; Wollesen de Jonge et al., 2021)
MSP + NO → CH$_3$SCH$_2$(O) + NO$_2$	4.9e-12*exp(260/T)	(Saunders et al., 2003)
MSP + CH$_3$O$_2$ → CH$_3$SCH$_2$(O) + O$_2$	3.74e-12	(Saunders et al., 2003)
CH$_3$SCH$_2$(O) → CH$_3$S + CH$_2$O	1.0e6	(Saunders et al., 2003)
CH$_3$S + O$_3$ → CH$_3$S(O) + O$_2$	1.15e-12*exp(430/T)	(Saunders et al., 2003)
CH$_3$S + O$_2$ → CH$_3$S(OO)	1.20e-16*exp(1580/T)	(Saunders et al., 2003)
CH$_3$S(O) + O$_3$ → CH$_3$(O$_2$) + SO$_2$	4.00e-13	(Saunders et al., 2003)
CH$_3$S(OO) → CH$_3$(O$_2$) + SO$_2$	5.60e16*exp(-10870/T)	(Saunders et al., 2003)
CH$_3$S(OO) → CH$_3$SO$_2$	1.00	(Saunders et al., 2003)
CH$_3$SO$_2$ + O$_3$ → CH$_3$SO$_3$ + O$_2$	3.00e-13	(Saunders et al., 2003)
CH$_3$SO$_2$ → CH$_3$(O$_2$) + SO$_2$	5.00e13*exp(-9673/T)	(Saunders et al., 2003)
CH$_3$SO$_3$ + HO$_2$ → MSA + O$_2$	5.00e-11	(Saunders et al., 2003)
CH$_3$SO$_3$ → CH$_3$(O$_2$) + H$_2$SO$_4$	5.00e13*exp(-9946/T)	(Saunders et al., 2003)

217 To examine the sensitivities of size-resolved aerosol formation and growth to DMS chemistry
218 modifications, model simulations are conducted as summarized in Table 5. Output from
219 simulations MOD and MOD_noHetLossHPMTF was then compared against simulation BASE to
220 understand the contribution of these additional chemical reactions on spatial pattern of the surface
221 concentration of major oxidation products of DMS.

222 **Table 5.** List of mechanisms used in GEOS-Chem-TOMAS simulations.

Model Runs	Mechanism	HPMTF Cloud Loss[*]	HPMTF Aerosol Loss[*]
BASE	All reactions from Table 1	-	-
MOD_noHetLossHPMTF	All reactions from Table 2-4	Off	Off
MOD	All reactions from Table 2-4	On	On

223 [*] Instantaneous formation of sulfate via HPMTF cloud and aerosol loss uses a reactive uptake co-efficient (γ) of
224 0.0016.

As shown in Table 2, the modified DMS chemistry simulations examined here include gas- and aqueous-phase oxidation of DMS and its intermediate oxidation products by OH, NO_3, O_3, and halogenated species as previously explored in an older version of GEOS-Chem (Chen et al., 2018). The aqueous-phase reactions in cloud droplets and aerosols were parameterized assuming a first-order loss of the gas-phase sulfur species (Chen et al., 2018). Further building upon this previous mechanism, the scheme used here also includes the formation and loss of HPMTF as previously tested in the global climate model CAM6-Chem as shown in Table 3 (Veres et al., 2020). Table 4 presents the third piece of the mechanism: a gas-phase MSA-producing branch of the H-abstraction pathway in the DMS chemistry bridging the other two sets of the reactions (Fung et al., 2022). A similarly integrated mechanism (Table 2-4) has been previously explored using the CAM6-Chem model with a focus on radiation budget impacts, with the exception of the DMS + NO_3 = MSP + HNO_3 reaction (included in Table 4) considered in this work (Fung et al., 2022; Novak et al., 2021; Wollesen de Jonge et al., 2021). We use a rate constant of 1.40×10^{-11} cm^3 molecules^{-1}s^{-1} for HPMTF + OH, which was previously determined based concentrations of other known sulfur species (DMS, DMSO, SO_2 and methyl thioformate; MTF; CH_3SCHO; a structurally similar proxy to HPMTF) and evaluated by box model (Jernigan et al., 2022a). An exploration of reaction rate uncertainty for the HPMTF+OH reaction (Table 3), including both high and low end limits of 5.5×10^{-11} cm^3 molecules^{-1}s^{-1} and 1.4×10^{-12} cm^3 molecules^{-1}s^{-1} resulted in only minor impacts on the fate of HPMTF and ultimate sulfate formation in our simulations (Novak et al., 2021; Wu et al., 2015).

Model sensitivity simulations were also performed with (case "MOD") and without HPMTF heterogeneous uptake to clouds and aerosols (case "MOD_noHetLossHPMTF") to account for how much of the DMS-derived HPMTF eventually forms SO_2 in the presence of these additional loss processes (Table 5). Previous work shows that aerosol surface chemistry causes additional decreases in HPMTF mixing ratios, primarily over land, and that the loss of HPMTF in clouds is larger (36%) than losses from aerosols (15%) when using an uptake coefficient of $\gamma = 0.01$ for both processes (Novak et al., 2021). In this work, based on recent laboratory measurements, we use a smaller uptake coefficient ($\gamma = 0.0016$) for HPMTF loss to aerosols and clouds (Table 5) (Jernigan et al., 2022b). We assume HPMTF directly produces sulfate in cloud and aerosol followed but previous work even though there is uncertainty in the fate of HPMTF heterogeneous loss (Zhang and Millero, 1993; Novak et al., 2021; Jernigan et al., 2022a). For the aqueous-phase reactions listed in Table 2, including the oxidation of intermediates DMSO and MSIA in cloud droplets and aerosols, a first-order loss of the gas-phase sulfur species was assumed following previously used parameterizations and physical parameter values (Chen et al., 2018). Alongside the gas-phase and aqueous-phase reactions relevant to the added DMS oxidation mechanism contributing to the formation of SO_2 and sulfate, the default version of GC-TOMAS used here also includes in-cloud oxidation of SO_2 by H_2O_2, O_3, and O_2 catalyzed by transition metals (Mn, Fe), as well as the loss of dissolved SO_2 by HOBr and HOCl, all of which are passed to TOMAS to account for sulfate production (Chen et al., 2017; Wang et al., 2021).

All simulations are conducted for the year 2018, which was chosen to match the model simulation with the dates of the NASA Atmospheric Tomography flight campaign (ATom-4) offering observational data for HPMTF, DMS and SO_2. Rate coefficients for all gas-phase sulfur reactions are obtained from the most recent JPL report and other references while sulfur product yields for gas-phase reactions are obtained from various laboratory and modeling studies (Burkholder et al., 2020; Lucas and Prinn, 2002; Hoffmann et al., 2016; Gershenzon et al., 2001; Kowalczuk et al.,

270 2003; Zhou et al., 2019; Jernigan et al., 2022a). The simulations included sea salt debromination
271 except for some sensitivity tests described below (Zhu et al., 2019; Schmidt et al., 2016). In all our
272 simulations including MOD, DMS is advected and undergoes chemical loss and transport but does
273 not undergo dry or wet deposition. However, dry and wet deposition of oxidation products such as
274 DMSO, MSIA, MSA and HPMTF are included.

275 We note that previous work has explored the impact of MSA on aerosol growth, including
276 modifications within TOMAS to represent this process (Hodshire et al., 2019). We do not include
277 this process here. Future work is recommended to examine its importance in the context of the
278 chemistry updates presented here.

3   Result and discussion

3.1 Model-Observations Comparison

3.1.1 Surface DMS mixing ratio

We compared the modeled DMS mixing ratio averaged for each month with the observational data collected at Crete Island (35° N, 26° E) and Amsterdam Island (37° S, 77° E) (Kouvarakis and Mihalopoulos, 2002; Chen et al., 2018; Castebrunet et al., 2009). Comparing simulations BASE and MOD, we find a closer match with DMS observations for simulations using modified DMS chemistry for both observation data shown in Figure 2. Modeled DMS mixing ratios calculated using base chemistry show strong positive bias during the months of May and June for Crete Island. By comparison, during the same period the modeled DMS mixing ratios calculated with modified chemistry reduces the bias from 102% to 44%. Similarly, for Amsterdam Island major overpredictions are apparent for the BASE simulation compared to MOD for the months of May-August. One reaction that may play a role in this shift is DMS + BrO, which as indicated earlier is responsible for a faster overall chemical loss of DMS, in particular over the southern hemisphere high latitudes. Beside DMS chemistry, sea surface DMS concentration is also proven to affect the modeled DMS mixing ratio (Chen et al., 2018). But the aim of this study is to investigate the chemistry aspect of DMS oxidation, so we did not explored how change in DMS seawater climatology and thus their emission influence the surface DMS mixing ratio.
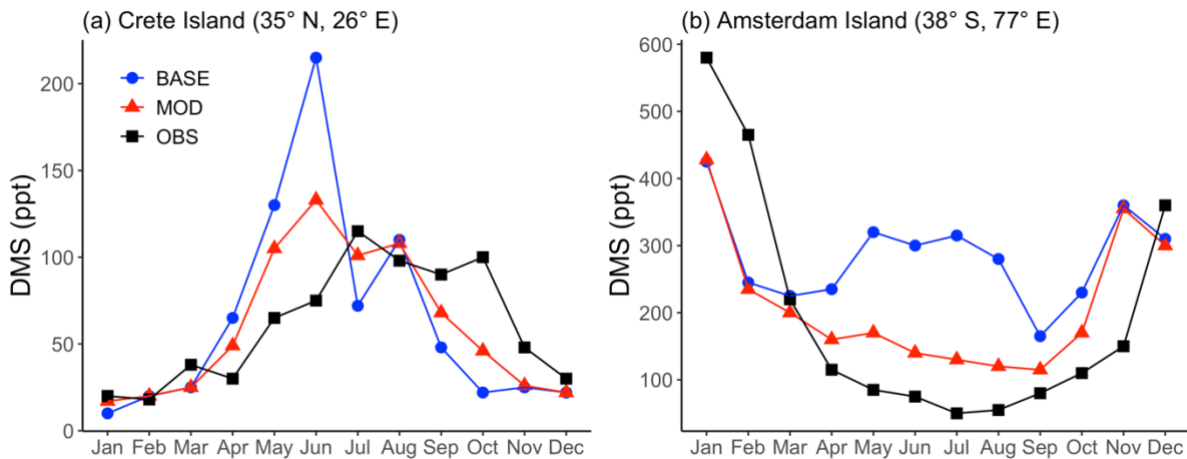
Figure 2 Observed (OBS) monthly mean surface DMS mixing ratios at (a) Crete Island and (b) Amsterdam Island compared with simulations BASE and MOD. Simulations are described in Table 5.

3.1.2 Comparison with aircraft observations

We further evaluate model output through a comparison with ATom-4 aircraft observations for specific days of measurement for DMS, HPMTF and SO_2 as shown in Figure 5. For this comparison, the model is sampled at the time and location of aircraft measurements by ATom-4 using the planeflight diagnostic of GEOS-Chem.
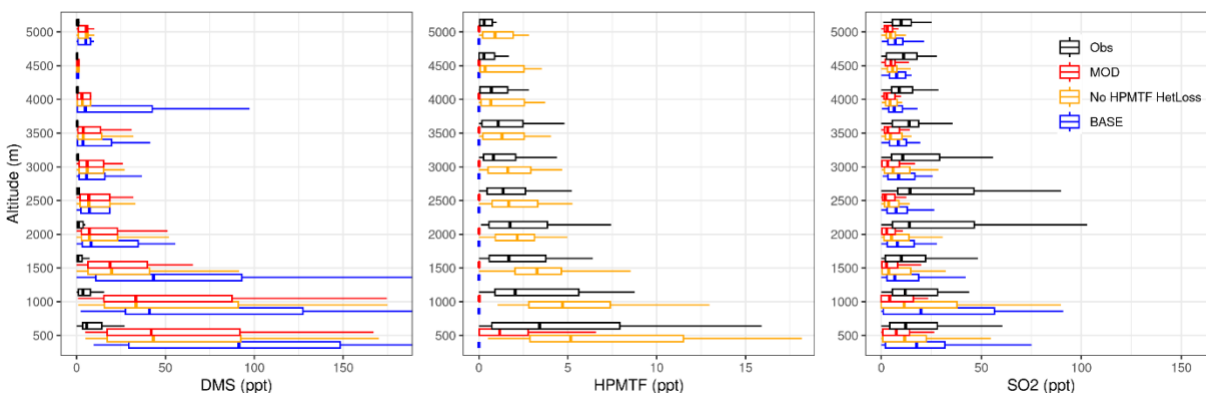
Figure 3 Vertical profiles of (a) DMS, (b) HPMTF and (c) SO$_2$ mixing ratios from ATom-4 observations (black) and model with simulation MOD sampled along the ATom-4 flight tracks (red) binned every 500 m of flight altitude. Also shown are modeled results without HPMTF heterogeneous loss with simulation MOD_noHetLossHPMTF (yellow), and for BASE GEOS-Chem chemistry (blue). Box plot whiskers show full range of distribution at each altitude bin. DMS observations are from Whole Air Samples (WAS) while HPMTF DC-8 observations are from iodide ion chemical ionization time-of-flight mass spectrometer (CIMS). SO$_2$ observations from ATom-4 campaign were measured by Laser Induced Fluorescence (LIF).

303   DMS concentrations measured during ATom-4 by whole air sampler (WAS) and modified
304   chemistry simulation values for nearest neighbor grid cells are shown in Figure 3a across different
305   altitude. In general, the modeled DMS concentrations are significantly higher than those observed
306   during ATom-4 missions especially close to the surface. However, model DMS concentrations
307   decrease more rapidly than the measurement with altitudes indicating vertical mixing could be one
308   of the underlying reasons for this trend. Even with this near surface bias, simulation MOD relative
309   to BASE has greater DMS losses and a shorter DMS lifetime (from 1.5 d to 1.0 d) reducing the
310   gap between modeled and observed concentration compared to simulation BASE. The reduction
311   in modeled DMS is largest over the Southern Ocean (shown later in Fig. 5b) where oxidation by
312   BrO and O$_3$ in the aqueous phase plays the major role in reducing DMS concentration, thereby
313   reducing the model-observation bias (Fig. 3b). Remaining model biases could be at least partially
314   attributed to model uncertainty in oxidant concentrations and cloud cover. The heterogeneous loss
315   of HPMTF has minimal impact on DMS concentration and its vertical profile.

316   For HPMTF, Figure 3b shows that the observed and modeled HPMTF concentrations remain
317   largely below 15 ppt. Agreement between observations and modeled HPMTF mixing ratios in the
318   vertical profile (Fig. 3b) is poor for simulation MOD even close to the surface. Removing all
319   heterogeneous loss of HPMTF improves model comparisons aloft, though surface concentrations
320   become overestimated (yellow line of Fig. 3b), showing a high sensitivity to cloud and aerosol
321   loss processes. We also find that the modeled HPMTF:DMS ratios range from 0.15:1 to 0.5:1 on
322   a daily basis in most cases for when there is no heterogeneous loss of HPMTF, compared to 0.5:1
323   observed during ATom-4 using the calibration maintained during measurement, implying
324   reasonably good agreement for this value over daily time scales (Veres et al., 2020). The SARP
325   flight campaign data has reported much lower HPMTF:DMS ratios (< 0.2) on cloudy days which
326   is relatable to modeled HPMTF with simulation MOD (Novak et al., 2021). For simulation MOD,
327   the modeled HPMTF:DMS ratio is 0.03:1 for until 0.5 km and then approaches zero with
328   increasing altitude, indicating the need for additional work to better constrain production and loss
329   processes of this intermediate. Our simulations indicate that cloud loss is the dominant modeled
330   removal process of HPMTF, consistent with previous findings, while gas-phase OH oxidation

331   plays a minor role (Novak et al., 2021). Thus, the addition of cloud uptake dramatically decreases
332   HPMTF concentrations throughout the troposphere. Overall, this allows only 7% of HPMTF
333   produced to end up as SO_2 with about 92% lost to clouds and aerosol and thus removed from the
334   system, resulting net reduction in mean global SO_2 by about 35%. Previous work focusing entirely
335   on gas-phase and heterogeneous loss of HPMTF shows a much higher bias for both DMS and
336   HPMTF during cloudy and clear sky conditions using the same model and a condensed DMS
337   oxidation mechanism, indicating that the addition of gas-phase and heterogeneous oxidation of
338   DMS including additional intermediates such as DMSO and MSIA further reduce model biases
339   for HPMTF with remaining overestimation of the multiphase loss for HPMTF (Novak et al., 2021).

340   We also compared the SO_2 concentrations measured during ATom-4 by Laser Induced
341   Fluorescence (LIF) and simulation MOD values for nearest neighbor grid cells are shown in Figure
342   3c across different altitude. Modeled surface SO_2 concentrations are lower than those observed
343   during ATom-4 missions across the vertical scale shown here for simulation MOD. The greater
344   SO_2 losses results in a shorter SO_2 lifetime (from 1.4 d to 1.3 d) for simulation MOD relative to
345   simulation BASE. The reduction in modeled SO_2 is largest over the Southern Ocean (shown later
346   in Fig. 7a) where heterogeneous oxidation of HPMTF is most efficient and irreversible. Removing
347   the heterogeneous loss of HPMTF increases the modeled SO_2 compared to simulation MOD with
348   underprediction remaining for altitudes > 1km. Remaining model biases could be at least partially
349   attributed to uncertainty in DMS oxidation processes along with other non-DMS sources
350   contributing high concentration of SO_2. Aside from uncertainty in DMS emissions and oxidation,
351   recent understanding of marine sulfur chemistry such as methanethiol (CH_3SH) oxidation has been
352   reported as an significant source of SO_2 in the marine atmosphere and could help reduce the bias,
353   a possibility deserving further investigation (Berndt et al., 2023; Novak et al., 2022). Overall the
354   DMS oxidation chemistry implemented in this work reduces the model observation bias close to
355   the surface (up to 1km) compared to BASE GEOS-Chem chemistry.

356   Besides the vertical profile shown in Figure 3b, the global mean surface mixing ratio of HPMTF
357   with simulation MOD_noHetLossHPMTF for May 2018 is plotted in Figure 4 and compared with
358   the observational measurement of HPMTF made during the ATom-4 mission during the NASA
359   DC-8 flight campaign, which sampled the daytime remote marine atmosphere over the Pacific and
360   Atlantic Oceans. The ATom-4 measurements were carried out during daytime hours between April
361   24 and May 21, 2018 for 21 non-continuous days.

362   For this campaign, flight patterns covered vertical profiles from 0.2 to 14 km above the ocean
363   surface. The flight leg duration was 5 minutes and boundary layer altitude of 150 to 200 m above
364   the ocean surface. Since most of these measurement days are within the month of May 2018, here
365   we compare observations with modeled output of mean surface concentration of HPMTF for this
366   month. With the rate of isomerization reaction used in previous work, we find spatial patterns of
367   monthly mean surface concentrations are generally well captured (Jernigan et al., 2022a). Overall,
368   we find that the simulation MOD_noHetLossHPMTF results in better agreement with existing
369   overprediction for the vertical profile (Fig. 3b) and global surface layer HPMTF levels (Fig. 4)
370   compared to previous modeled approaches using the CAM-chem model (Veres et al., 2020).
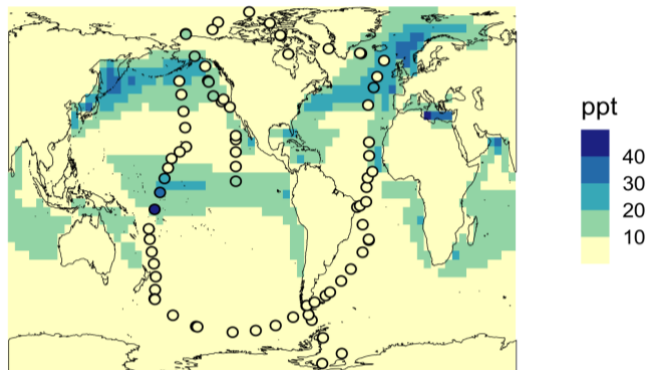
Figure 4 Geographic distribution of May 2018 monthly mean surface-layer mixing ratio of HPMTF for simulation MOD_noHetLossHPMTF mechanism represented for May 2018. The circles represent measurements of HPMTF during the ATom-4 mission by NASA DC-8 flight tracks with a limit of detection <1 ppt.

371

372 3.2 DMS burden and oxidation pathways

373 We find that the global burden of DMS in the MOD simulation is 67 Gg S (Table B1), 38% lower
374 than what we find with the simulation BASE (108 Gg S). Even with this 38% reduction, global
375 burdens are still well within the range of 9.6–150 Gg S suggested in other studies (Faloona, 2009;
376 Kloster et al., 2006). Figure 5a shows that surface DMS mixing ratios are highest in the North
377 Pacific and North Atlantic oceans for June-July-August (JJA) and in the Southern Ocean during
378 the months of December-January-February (DJF), revealing the underlying seasonality of DMS
379 emissions. According to previous studies, the highest DMS concentrations usually occur in
380 summer months due to higher rates of primary production in the presence of adequate solar
381 irradiation and high temperatures for both hemisphere (Galí et al., 2018; Lana et al., 2011; Wang
382 et al., 2020). In simulation MOD, the global mean surface-layer DMS burden was higher in SH
383 for DJF and lower in NH for JJA which is due to larger ocean area in the SH than NH. We also
384 find that the reactions of this expanded DMS oxidation mechanism collectively contribute to
385 reductions in mean surface-layer DMS concentration of 60% and 23% compared to BASE for JJA
386 and DJF respectively (Fig. 5b). These reductions are due primarily to the addition of multiple new
387 chemical loss pathways compared to BASE, which are especially impactful during JJA months
388 due to due to elevated BrO in the SH winter and also higher O_3 and OH concentration in the NH
389 summer compared to the SH summer (Zhang et al., 2018; Pound et al., 2020).
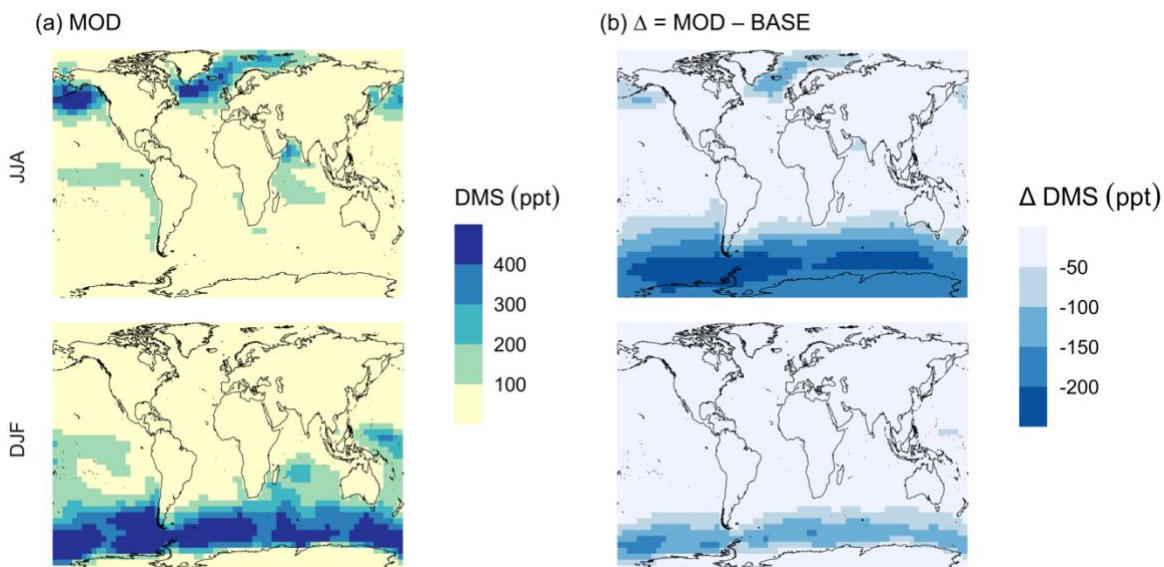
Figure 5 Geographic distribution of mean surface DMS mixing ratio (ppt) for simulation (a) MOD and (b) difference between simulations from its baseline, Δ = MOD – BASE from GEOS-Chem simulations. Here, JJA and DJF represent June-July-August and December-January-February respectively. Simulations are described in Table 5.

As shown in Fig. 5b, this DJF DMS reduction is seen mainly over the Southern Ocean and is largely attributable to faster chemical losses through the added reactions of DMS + BrO and $DMS_{(aq)} + O_{3(aq)}$, which in earlier work was hypothesized as a possible reason for high model biases in the absence of detailed halogen chemistry (Chen et al., 2016). The global lifetime of DMS decreases from 1.5 days in the BASE simulation to 1.0 day in the MOD simulation.

These values are comparable to the range of 0.8–2.1 d reported by previous studies (Chen et al., 2018; Fung et al., 2022). The global DMS emission flux (F_{DMS}) from ocean to the atmosphere is 22 Tg S yr^{-1} and is within the range of 11– 28 Tg S yr^{-1} simulated by GEOS-Chem and other models in previous studies (Lennartz et al., 2015; Fung et al., 2022; Chen et al., 2018; Hezel et al., 2011; Spracklen et al., 2005). Our F_{DMS} is higher than the 18 Tg S yr^{-1} which uses sea surface DMS concentration from Kettle et al. (1999) as reported (Chen et al., 2018) indicating the DMS emission varies with change in sea surface DMS climatology. The analysis and improvement of DMS emissions directly is not a part of this work, but we note that improved and validated inventories for DMS will certainly play a role in subsequent oxidation product comparisons. We recommend ongoing evaluation of DMS emissions inputs to complement the expanded chemical mechanism development we present here.

In the BASE simulation the chemical loss of DMS acts as its only sink (as opposed to dry and wet deposition), leading to a full conversion yield of DMS into SO_2 (82.5%) and MSA (17.5%) (Fig. A3a). Figure 6 shows that in simulation MOD with updated DMS oxidation scheme DMS is mainly oxidized by OH in the gas phase, with 33.5% of losses proceeding via the H-abstraction channel and 29.4% via the OH-addition pathway, together contributing up to 62% of global average loss with high regional contribution over the tropical oceans via the abstraction channel where surface OH is the highest. NO_3 oxidation of DMS accounts for another 12.8% of global DMS chemical losses, comparable to values found in previous studies (Chen et al., 2018; Fung et

414 al., 2022). Over the ocean, the NO_3 loss pathway is strongest in the NH coastal regions due to
415 outflow of NO_x sources from over the land whereas for the SH values are generally less than 10%.
416 Oxidation by BrO is responsible for 19.6% of the global DMS removal, falling within the
417 previously estimated range of 8%–29% (Boucher et al., 2003; Khan et al., 2016; Chen et al., 2018).
418 Regionally, its contribution can reach 50%–60% over high latitudes of the Southern Hemisphere
419 as well as to the north near the Arctic Ocean, consistent with previous box model studies based on
420 the availability of high BrO and low OH and NO_3 for those regions (Hoffmann et al., 2016). DMS
421 $+ O_3$ accounts for 2.7% (aqueous) and 1.1% (gas phase) of global surface DMS loss. The higher
422 contribution from BrO and lower from O_3 using this mechanism compared to some previous
423 studies could be explained in part by the recently implemented sea-salt debromination mechanism
424 in GEOS-Chem, resulting in a much higher background level of BrO as well as lower O_3
425 abundance, especially in the southern hemisphere (Boucher et al., 2003; Chen et al., 2018; Fung
426 et al., 2022; Sherwen et al., 2016a; Wang et al., 2021). To further quantify the importance of the
427 sea salt debromination mechanism, we perform an emissions sensitivity test by turning this
428 emission source off while using updated MOD chemistry (Fig. A1). As would be expected, these
429 simulations show much lower BrO formation (as shown in Fig. A6) and resulting chemical
430 impacts, with overall oxidation contributions comparable to previous literature (Schmidt et al.,
431 2016; Wang et al., 2021). We find that under this scenario the relative contribution of BrO for
432 DMS loss decreases to 3.8%, while the DMS $+ O_3$ pathway increases to 4.0% (aqueous) and 1.8%
433 (gas phase), and the DMS + OH pathway increases to 38.0% (abstraction) and 36.1% (addition)
434 of global surface DMS loss (Fig. A1). The DMS loss via interaction with NO_3 also increases by
435 2.5% when sea salt debromination is turned off in the mechanism. The relative contributions of
436 other oxidants remain mostly unaffected in the BrO sensitivity test.
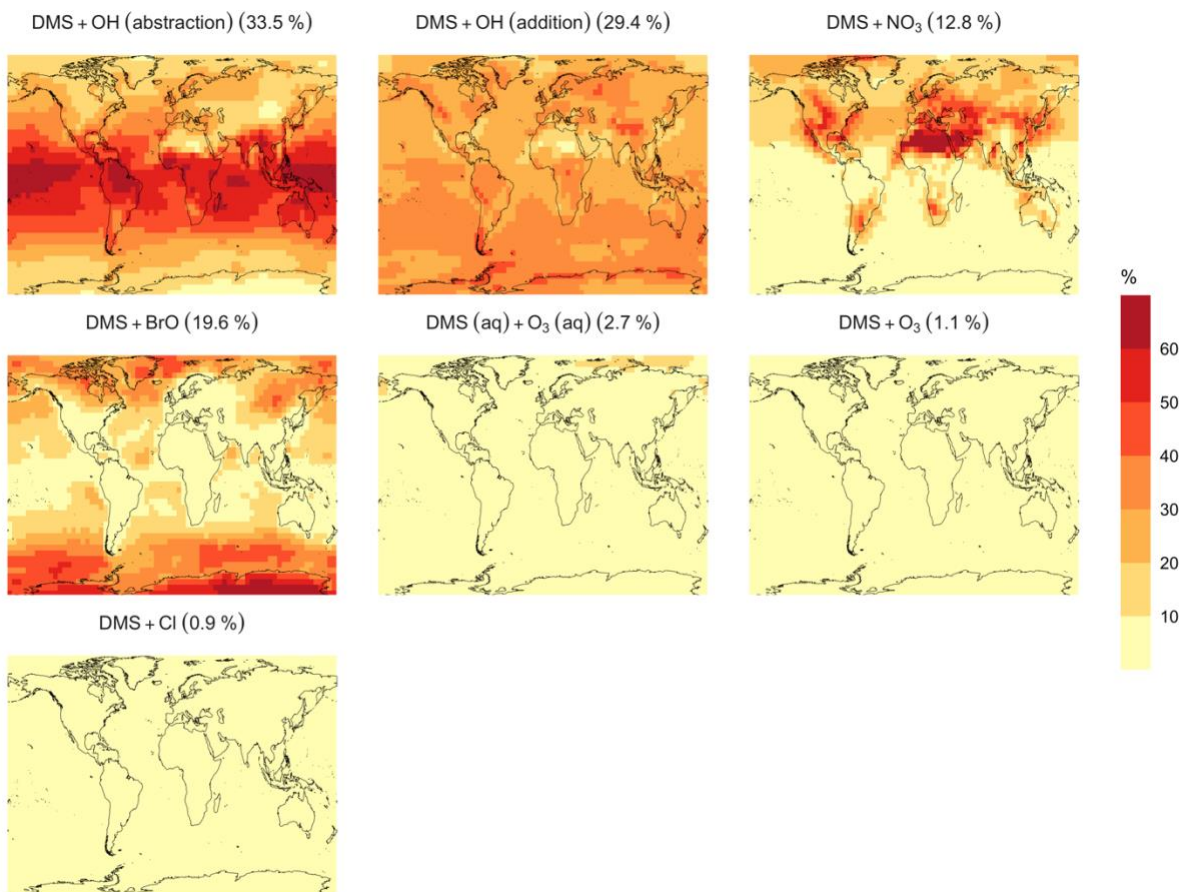
Figure 6 Geographic distribution of the annual mean surface layer fraction of total DMS oxidation (percent) attributed to different tropospheric oxidants for simulation MOD (described in Table 5). Percentages in parentheses indicates average contribution to global chemical loss for fraction of DMS emitted for each reaction pathways presented here.

Regionally, the fractional contribution of aqueous-phase DMS + O_3 to DMS oxidation can be up to 10%–20% over high-latitude oceans, which is in the middle of the 5%–30% contribution to high-latitude DMS losses previously reported (Chen et al., 2018; Fung et al., 2022; von Glasow and Crutzen, 2004). The Cl oxidation reaction contribute about 0.9% and 1.0% respectively for with and without sea salt debromination to the chemical removal of DMS, consistent with some previous studies (Atkinson et al., 2004; Fung et al., 2022). This does differ from other reported values however, including those from a global model study (4%) and box model simulations (8% –18%) (Chen et al., 2018; Hoffmann et al., 2016; von Glasow and Crutzen, 2004). It's worth noting that none of the studies reporting such high Cl contributions included HPMTF formation and loss. Ongoing uncertainties associated with model-observation bias of Cl should be further resolved to get better representation of halogenated species contributions to DMS loss (Wang et al., 2021). Due to slower reaction kinetics and lower fractional contribution reported earlier compared to BrO with DMS and uncertainty in surface concentration and kinetics for photochemically generated halogenated species such as Br, IO we did not include them in our chemical scheme (Chen et al., 2018).

3.3 Implications of the extended DMS oxidation mechanism

453 Figure 7 shows that the MOD simulation results in 35% reduction of surface layer SO_2 relative to
454 BASE, but a huge increase in SO_4^{2-} in most regions. These changes suggest that the combination
455 of gas-phase and aqueous-phase reactions results in a higher net yield of MSA and HPMTF and a
456 lower net yield of gas-phase SO_2. Additionally, comparison of simulation MOD relative to
457 MOD_noHetLossHPMTF (Fig. A2a) shows that loss of HPMTF in cloud droplets and aerosol
458 reduces the global mean production of SO_2 by 19.6%, contributing to the SO_2 reduction and
459 increasing mean surface layer sulfate by 16.1% (Fig. A2b). This reduction in SO_2 is expected to
460 reduce the availability of gas-phase sulfuric acid for new particle formation by nucleation (Clarke
461 et al., 1998a). Total SO_4^{2-} increases over the ocean, however, because the increased SO_4^{2-}
462 production from rapid loss of MSA and HPMTF in aqueous-phase offsets the reduced oxidation
463 of SO_2 (Fig. 7b).
464
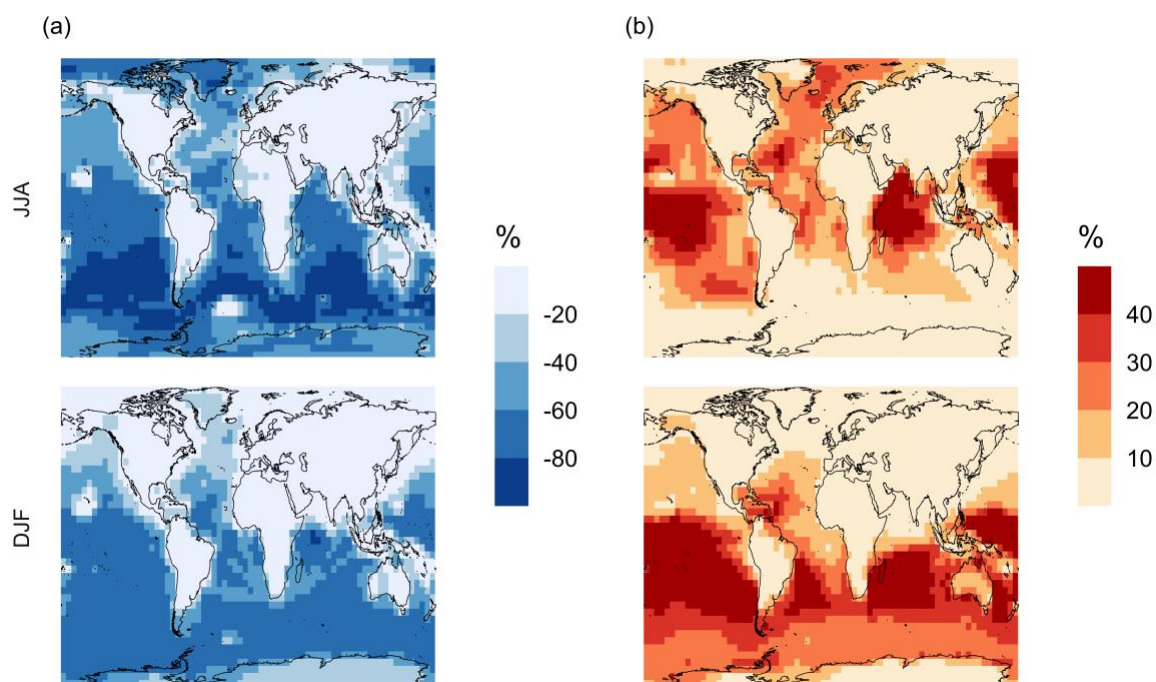
Figure 7 Percent change in simulated surface layer (a) SO_2 and (b) SO_4^{2-} for simulation MOD relative to BASE for June, July and August mean (JJA) and December, January, and February mean (DJF). Simulations are described in Table 5.

465 Qualitatively, the regions showing the highest percent changes of SO_2 are consistent with previous
466 studies that included HPMTF chemistry and loss processes though the extent of this reduction is
467 much higher with the integrated mechanism used in our study (Fig. 7a) (Novak et al., 2021). The
468 regions with the largest percent change in SO_2 reduction are those where DMS oxidation
469 contributes most to SO_2, and where HPMTF production and in-cloud oxidation of HPMTF are
470 efficient. This spatial pattern thus helps us to identify where the production and heterogeneous loss
471 of HPMTF and MSA is enhanced. One of the reactions that possibly contributes to delayed
472 formation and reduction of SO_2 concentration is the first-generation OCS formation from OH
473 oxidation of HPMTF. We find that addition of cloud and aerosol loss significantly decreases the
474 OCS production, especially in high cloud cover regions as previously reported (Jernigan et al.,
475 2022a). Even though the cloud loss of HPMTF increases the production of surface sulfate, the total

global sulfate burden we calculate increases by only 4.1% from the BASE sulfate burden of around 575 Gg S. This can be attributed to minor contribution of DMS and its intermediate oxidation products in SO_2 production compared to other non-DMS derived sources. In addition, the production of stable intermediate oxidation products delay the conversion of SO_2 to SO_4^{2-} and modify its spatial distribution in the marine environment. Thus, we should expect these aqueous phase oxidation products to contribute to particle mass rather than increase the number of nucleated particles, as suggested in other studies (Clarke et al., 1998b; Novak et al., 2021; Williamson et al., 2019).
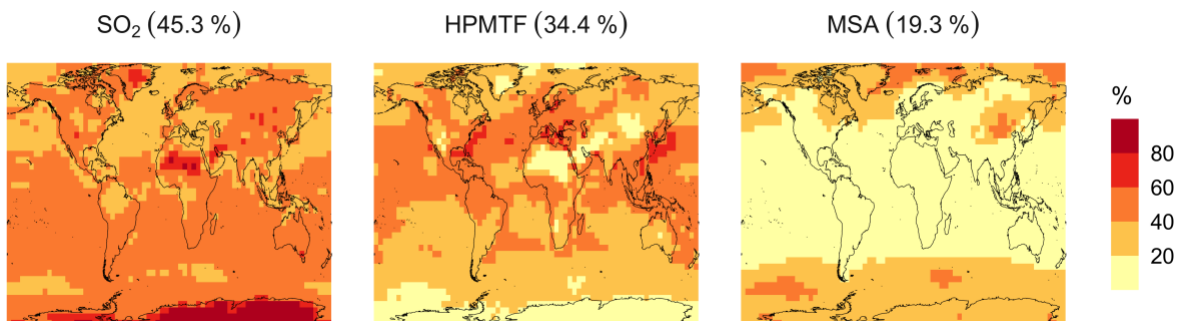
Figure 8 Simulated branching ratio (in %) of the DMS oxidation mechanism considering SO_2, HPMTF and MSA as major terminal oxidation products calculated from their annual total production rate for simulation MOD.

The spatial distribution of product branching ratios of DMS oxidation is shown in Figure 8. Here, 34.4% of the annual total DMS oxidation will end up as HPMTF, while final SO_2 yield decreases to 45.3% compared to 82.5% for the BASE simulation (Fig. A3a). The terminal HPMTF branch represents sulfur removed from the system by cloud and aerosol uptake of HPMTF, leading to a reduced overall formation of SO_2. With sea salt debromination turned off, modified chemistry forms even more HPMTF (41.7%), slightly higher SO_2 (46.4%), and lowers the yield of MSA to 11.9% (19.3% with the sea salt debromination on), underscoring the importance of halogen chemistry for MSA production (Fig. A3b). These results are broadly consistent with observationally constrained estimates from ATom-4 flight campaigns, where ∼ 30% - 40% DMS was oxidized to HPMTF along their flight tracks compared to 34.4% for the full branch of HPMTF in the present work, as well as with previous modeling studies showing 33% HPMTF formation as terminating product (Veres et al., 2020; Fung et al., 2022). MSA is produced mostly by aqueous phase oxidation of MSIA by O_3 and OH according to the mechanism used here and has high abundance near the Southern Ocean and Antarctic belt as reported by previous studies (Chen et al., 2018; Hoffmann et al., 2016; Fung et al., 2022). The global burden of MSA decreases dramatically, from 19 Gg S for 'Base' to 8.5 Gg S for simulation MOD. The higher rate of major loss process or lower rate of production of MSA from the aqueous phase reactions could be responsible for this reduction in global budget (Fung et al., 2022).

3.4 Impact on aerosol size distributions

Following the percent change in simulated surface layer SO_2 and SO_4^{2-} for modified DMS chemistry (Fig. 7), we further explore how this expanded DMS oxidation chemistry impacts modeled aerosol size distributions. Figure 9 shows the global mean surface-layer percent change in the normalized aerosol number concentration for modified chemistry relative to the BASE simulation, with and without cloud and aerosol HPMTF loss processes. The aerosol number

509 concentration decreases for the sub-80 nm diameter size bins for both simulations, especially
510 during the DJF months when cloud and aerosol loss pathways of HPMTF are included (MOD
511 case), demonstrating the negative impact of these processes on simulated new particle formation.
512 Without these processes included (as in case MOD_noHetLossHPMTF), percent changes are far
513 more modest for these smaller size ranges. On the other hand, HPMTF lost to clouds and aerosols
514 increases the simulated number of particles with diameter above 100 nm in the MOD simulation,
515 consistent with the increase in sulfate mass concentrations shown in Fig. 7 and suggesting that
516 HPMTF heterogenous loss promotes simulated particle growth to diameters larger than 80-100
517 nm. The greater abundance of particles larger than 100 nm also acts as a condensation sink, further
518 suppressing nucleation and growth at smaller size ranges.
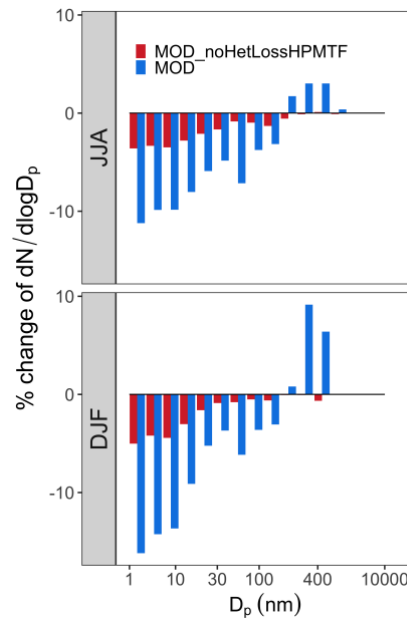
Figure 9 Global mean surface-layer percent change in normalized aerosol number concentration for different size bins with particle diameter, D_p in the range of 3 nm $< D_p <$ 10000 nm for simulations MOD and MOD_noHetLossHPMTF relative to simulation BASE. Simulations are described in Table 5.

519 The geographic distribution of surface layer aerosol number concentration for aerosol in the size
520 range of 3 – 80 nm for two seasons is shown in Figure 10. We find that global mean aerosol number
521 concentration in this size range decreases for simulations MOD and MOD_noHetLossHPMTF
522 relative to BASE by 12.8% and 9.9% respectively. Decreases are greater for simulation MOD (Fig.
523 10b). Fig. 10c shows the effect of HPMTF heterogenous loss processes on the number of particles
524 with diameters between 3-80 nm for simulation MOD relative to simulation
525 MOD_noHetLossHPMTF. The largely negative impact of HPMTF loss to clouds and aerosols on
526 sub-80 nm particle number is contributed to by enhanced direct sulfate formation on pre-existing
527 particles, bypassing gas-phase SO_2 formation (a precursor for new particle formation). As well, in
528 the model, new particles grow through condensation of H_2SO_4 and organics and their growth are
529 dependent on the condensation sink, while loss of particle number depends on the coagulation
530 sink. Thus, changes to the condensation/coagulation sinks and sulfuric acid production rate
531 through the updated mechanism will also alter the growth rates of small particles (sub-80 nm) as
532 well as their coagulation loss rates. Hence, similar to the discussion for Figure 9, the reduction of
533 gas-phase production of H_2SO_4 in MOD relative to BASE slows new-particle formation and

534 growth, while the additional production of sulfate through aqueous chemistry on larger particles
535 in MOD increases the coagulational scavenging of the newly formed particles. These two effects
536 synergistically reduce the concentration of ultrafine particles in the model. The fraction of newly
537 formed particles that can reach the CCN size is dependent on the particle growth rates, especially
538 for particle sizes below 10 nm, where we see highest coagulation losses to larger particles. The
539 sensitivity of these results to the new sea salt debromination parameterization is shown in Fig. A4,
540 where we find a regional increase in aerosol number concentration at mid to higher latitude of the
541 SH despite low BrO concentrations (Fig A4).
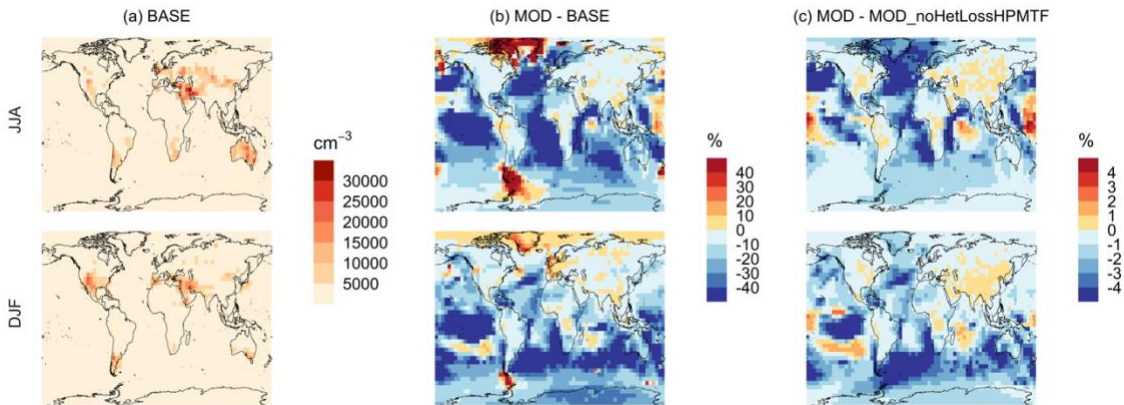
Figure 10 Geographic distribution of seasonal-mean surface-layer aerosol number concentration in cm^{-3} (for particles with diameters between 3 – 80 nm) for (a) the BASE simulation, (b) the percent difference between MOD and BASE and (c) the percent difference between MOD and MOD_noHetLossHPMTF to show the role of cloud and aerosol loss of HPMTF. Simulations are described in Table 5.

542
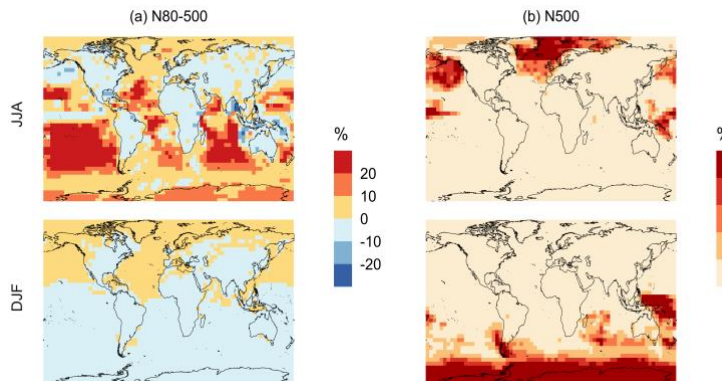
Figure 11 Geographic distribution of percent difference in seasonal-mean surface-layer aerosol number concentration in cm^{-3} for simulations MOD relative to simulations BASE for diameters between (a) 80 – 500 nm and (b) >500 nm. Simulations are described in Table 5.

543 Finally, we also analyze the impact of this expanded DMS scheme on particles larger than 80 nm
544 (Fig. 11). We find increases of around 6.6% for JJA mean surface layer number concentration of
545 aerosol with diameters between 80-500 nm, while DJF months show mean reductions of -5.4% for
546 DJF despite largely positive changes in the marine NH for these months (Fig. 11a). However, for
547 the > 500 nm size ranges (Fig. 11b), the global mean surface layer number concentration of aerosol
548 mostly increases, with highest changes occurring in the areas of peak DMS emission in both
549 hemispheres, during their summertime season. A similar trend is observed in the absence of cloud
550 and aerosol HPMTF uptake in simulation MOD_noHetLossHPMTF (Fig. A5).

551   Comparing the regional extent and direction of this change, we find the net increase in particle
552   number concentration is higher for MOD compared to MOD_noHetLossHPMTF, highlighting the
553   importance of HPMTF loss processes to clouds and aerosols as a contributor of CCN.
554

4   Conclusion

In this study we update the default DMS oxidation scheme in the GEOS-Chem model by implementing an integrated oxidation mechanism. The new scheme includes gas-phase and aqueous phase reactions involving DMSO, MSIA and HPMTF formation, as well as newly identified HPMTF loss processes yielding considerable changes in seasonal concentrations of major oxidation products and sulfur-derived aerosols. With this new chemistry scheme, global annual mean surface DMS concentration decreases by 38% relative to the BASE scheme in GEOS-Chem globally due to the presence of additional loss processes in the integrated mechanism reducing the bias to ATom-4 DMS measurement.

In this new scheme, OH, BrO, O_3 and NO_x species act as important sinks of DMS contributing to 62.9%, 19.6%, 3.8% and 12.8% global annual mean surface DMS loss, highlighting the relative importance of these loss process in determining surface DMS budget. We also find that at higher latitudes, gas phase and multiphase oxidation of DMS by O_3 and BrO becomes important to determine the budget of DMS. On the other hand, at lower latitudes OH contribute to a greater extent compared to other sinks and at comparable extent to previous studies exploring this chemistry. For the global distribution of simulated HPMTF, our updated scheme in GEOS-Chem provides a reduced high bias against observations compared to previous studies. While emissions of BrO are uncertain in this version of GEOS-Chem, we find that the compound acts as a key sink of DMS, especially over the Southern Ocean. Overall, we find large reduction in SO_2 (35%) and an increase in sulfate (22%) due to the addition of heterogeneous HPMTF loss processes.

The lower SO_2 with the new DMS chemistry scheme contributes to a reduction in the global annual mean surface layer number concentration of particles with diameters less than 80 nm by 12.8%, contributed to by reductions in gas-phase precursors for new particle formation. There is a concurrent increase of 3.1% in the global annual mean number of particles with diameters larger than 80 nm. This latter global mean particle number change varies in sign seasonally, with a 6.6% increase for JJA, and a 5.4% decrease for DJF. This decrease is dominated by southern hemisphere summertime changes, connected with suppressed new particle formation/growth and enhanced coagulation following additional sulfate production through aqueous chemistry. Cloud loss processes related to HPMTF make key contributions to these simulated changes through enhancement of aqueous-phase particle growth of those particle large enough to act as CCN.

Although the increased chemical mechanism complexity described in this work will necessarily increase model computational cost (MOD simulation run times increase by approximately 16%), this study highlights the value of including a more realistic chemical oxidation mechanism of DMS and its stable intermediates for better representation of DMS-derived aerosol in the marine atmosphere, as well as its seasonal size distributions. A reduced form of the key chemical species and pathways should be able to capture the key processes with less computational impact and will be a priority in future work.

Appendix A: Additional figures
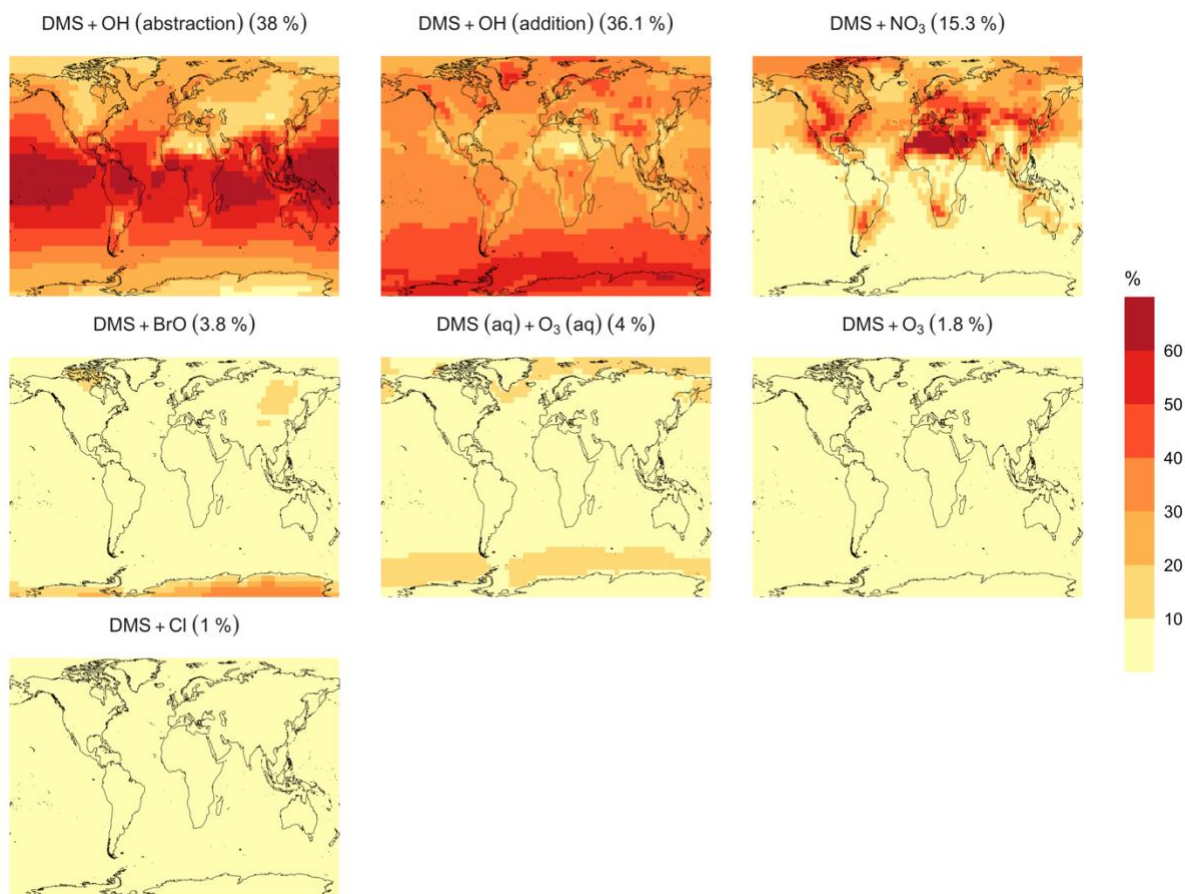
Figure A1 Surface layer geographic distribution of the simulated annual mean fraction of total DMS oxidation (percent) attributed to different tropospheric oxidants for a simulation otherwise the same as simulation MOD except with no sea salt debromination. Percentages in parentheses indicates average contribution to global chemical loss as a fraction of DMS emitted for each reaction pathways presented here. Simulations are described in Table 5.

593
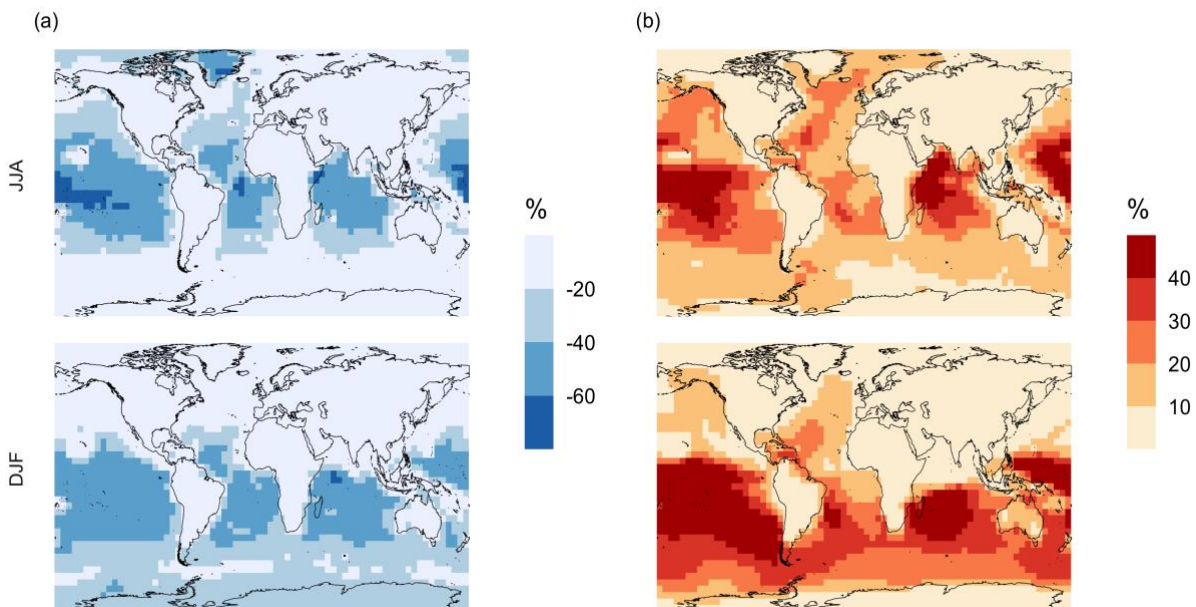
Figure A2 Percent change in simulated surface layer (a) SO_2 and (b) SO_4^{2-} for simulation MOD relative to MOD_noHetLossHPMTF for June, July and August mean (JJA) and December, January, and February mean (DJF). Simulations are described in Table 5.

594
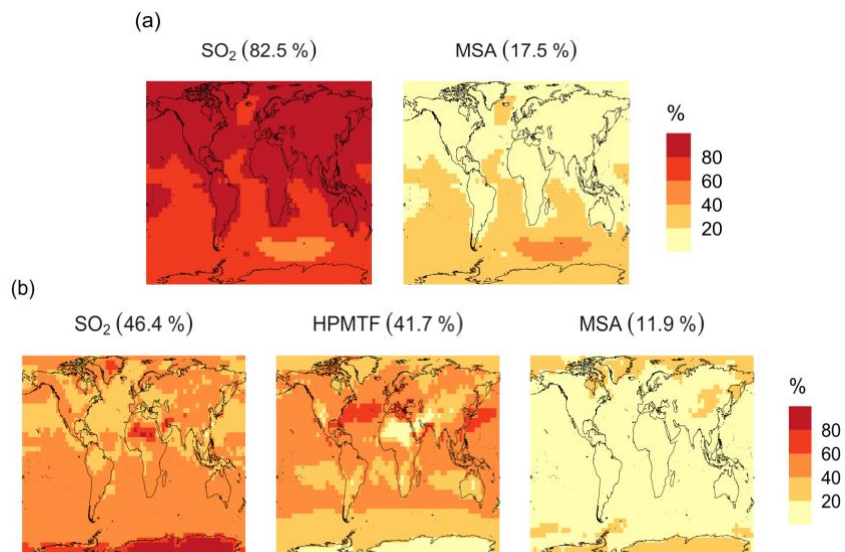
Figure A3 Simulated annual mean surface layer branching ratios (in %) of the DMS oxidation mechanism considering SO_2, HPMTF, and MSA as major oxidation products calculated from their total production rates for simulations similar to (a, top row) BASE and (b, bottom row) MOD, except all with no sea salt debromination. Simulations are described in Table 5.

595
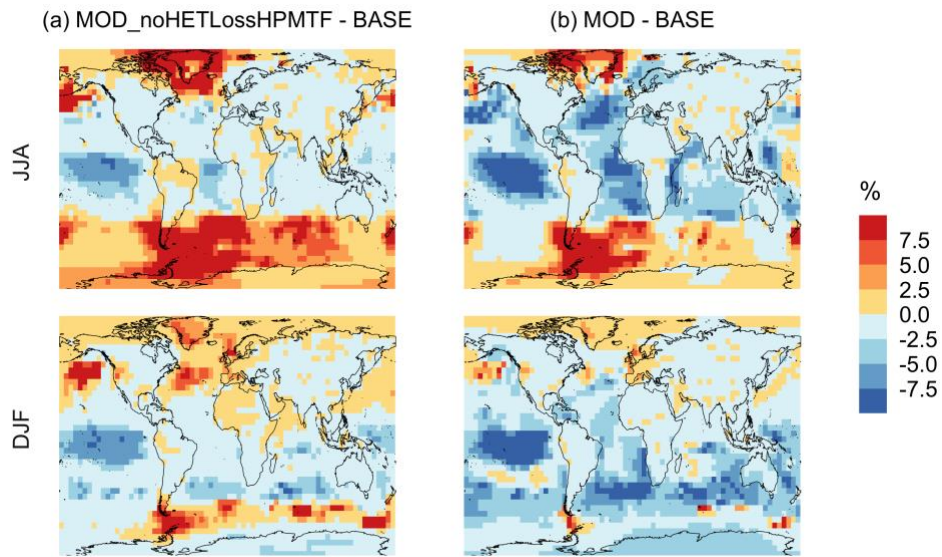
Figure A4 Geographic distribution of percent difference in seasonal-mean surface-layer aerosol number concentration in cm-3 (for particles with diameters between 3 – 80 nm) for simulations similar to (a) MOD_noHetLossHPMTF and (b) MOD relative to simulations BASE, except all with no sea salt debromination. Simulations are described in Table 5.

596
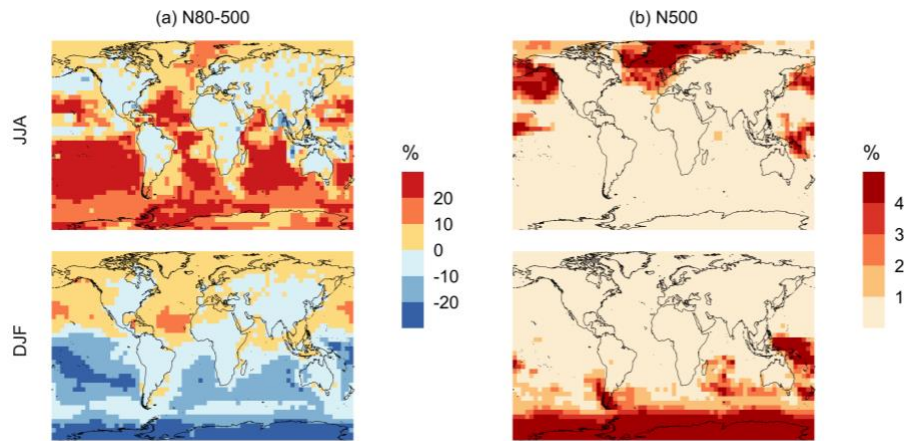
Figure A5 Geographic distribution of percent difference in seasonal-mean surface-layer aerosol number concentration in cm-3 for simulations similar to MOD_noHetLossHPMTF relative to simulations BASE, for particle diameters between (a) 80 – 500 nm and (b) > 500 nm. Simulations are described in Table 5.

597
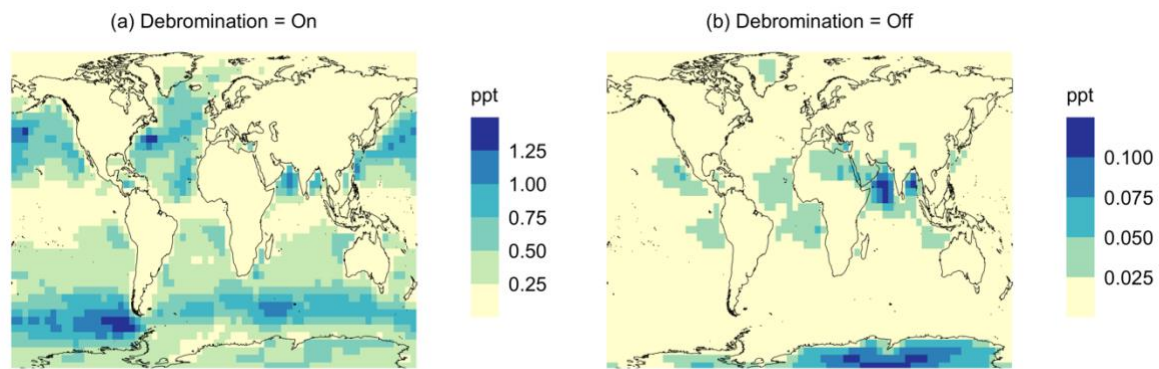
Figure A6 Geographic distribution of mean surface BrO mixing ratio (ppt) for (a) with sea salt debromination and (b) without sea salt debromination for simulation MOD. Simulations are described in Table 5.

598
599

Appendix B: Additional Table

Table B1. Global atmospheric flux, deposition, burdens, lifetime of DMS and its oxidation products, chemical loss rates for specific reaction pathways and global mean concentration of major oxidants are listed here for the case of simulation MOD. Note that SO_2 and SO_4^{2-} includes natural as well as anthropogenic sources.

F_{DMS} (Gg S yr^{-1})	2.2×10^4
Deposition of MSA (Gg S yr^{-1})	3.6×10^3
Deposition of HPMTF (Gg S yr^{-1})	9.1×10^1
Deposition of DMSO (Gg S yr^{-1})	1.7×10^3
Deposition of MSIA (Gg S yr^{-1})	2.2×10^2
DMS (GgS)	67
MSA (GgS)	8.5
HPMTF (GgS)	0.75
SO_2 (GgS)	261.5
SO_4^{2-} (GgS)	598.6
τ_{DMS} (d)	1.0
τ_{MSA} (d)	0.8
τ_{HPMTF} (d)	0.7
τ_{SO2} (d)	1.3
τ_{SO4}^{2-} (d)	4.4
DMS lost to MSA (Gg S yr^{-1})	4.1×10^3
DMS lost to HPMTF (Gg S yr^{-1})	7.6×10^3
DMS lost to SO_2 (Gg S yr^{-1})	9.2×10^3
MSA lost to particle growth (Gg S yr^{-1})	4.3×10^2
HPMTF lost to SO_2 (Gg S yr^{-1})	4.5×10^2
HPMTF lost to cloud (Gg S yr^{-1})	6.7×10^3
HPMTF lost to particle growth (Gg S yr^{-1})	2.7×10^2
OH (molec cm^{-3})	1.1×10^6
Cl (molec cm^{-3})	4.5×10^7
NO_3 (molec cm^{-3})	2.0×10^{12}
O_3 (molec cm^{-3})	4.4×10^{16}
BrO (molec cm^{-3})	6.3×10^{11}

Data availability. The DMS observational data in Fig. 2 were obtained from the referenced papers (Kouvarakis and Mihalopoulos, 2002; Castebrunet et al., 2009). The observations data during ATom-4 are published through the Distributed Active Archive Center for Biogeochemical Dynamics (DAAC) at (Novak et al., 2021; Wollesen de Jonge et al., 2021), https://doi.org/10.3334/ORNLDAAC/1921 and https://daac.ornl.gov/ATOM/guides/ATom_SO2_LIF_Instrument_Data.html.

Author contributions. LT and WCP designed the research goals, aims, and methodology, implemented the new code into GC-TOMAS. QC, BA, CHF and CDH contributed in code development. All authors provided expert advice on data analysis, interpretation, and visualization. LT ran model simulations, analyzed the data, created the figures, and led manuscript development and editing.

Competing interests. The contact authors have declared that none of the authors has any competing interests.

Acknowledgements. LT and WCP gratefully acknowledge Ka Ming Fung for discussions on DMS oxidation chemistry. BC thanks Rachel Y.-W. Chang for discussions on marine aerosols.

Financial support. LT and WCP was supported by NSF grant no. 2155192. QC was supported by the Hong Kong Research Grants Council (Grant No. 15223221 and 15219722). BA was supported by NSF AGS 2109323 and PLR 1904128. CHF was supported by NASA FINESST (grant 80NSSC19K1368). CDH acknowledges funding support from NSF AGS (grant 1848372). BC gratefully acknowledges research funding supported by the Ocean Frontier Institute, through an award from the Canada First Research Excellence Fund. JRP was supported by the Atmospheric System Research (ASR) program, part of the US Department of Energy's Office of Biological and Environmental Research within the Office of Science, under grant DE-SC0021208. SI was supported by Ferring Pharmaceuticals through the Extreme Environments research Laboratory, École Polytechnique Fédérale de Lausanne (EPFL).

References

Adams, P. J. and Seinfeld, J. H.: Predicting global aerosol size distributions in general circulation models, J. Geophys. Res. Atmospheres, 107, AAC 4-1-AAC 4-23, https://doi.org/10.1029/2001JD001010, 2002.

Alexander, B., Park, R. J., Jacob, D. J., Li, Q. B., Yantosca, R. M., Savarino, J., Lee, C. C. W., and Thiemens, M. H.: Sulfate formation in sea-salt aerosols: Constraints from oxygen isotopes, J. Geophys. Res. Atmospheres, 110, https://doi.org/10.1029/2004JD005659, 2005.

Alexander, B., Park, R. J., Jacob, D. J., and Gong, S.: Transition metal-catalyzed oxidation of atmospheric sulfur: Global implications for the sulfur budget, J. Geophys. Res. Atmospheres, 114, https://doi.org/10.1029/2008JD010486, 2009.

Amos, H. M., Jacob, D. J., Holmes, C. D., Fisher, J. A., Wang, Q., Yantosca, R. M., Corbitt, E. S., Galarneau, E., Rutter, A. P., Gustin, M. S., Steffen, A., Schauer, J. J., Graydon, J. A., Louis, V. L. S., Talbot, R. W., Edgerton, E. S., Zhang, Y., and Sunderland, E. M.: Gas-particle partitioning of atmospheric Hg(II) and its effect on global mercury deposition, Atmospheric Chem. Phys., 12, 591–603, https://doi.org/10.5194/acp-12-591-2012, 2012.

Atkinson, R., Baulch, D. L., Cox, R. A., Crowley, J. N., Hampson, R. F., Hynes, R. G., Jenkin, M. E., Rossi, M. J., and Troe, J.: Evaluated kinetic and photochemical data for atmospheric chemistry: Volume I - gas phase reactions of O_x, HO_x, NO_x and SO_x species, Atmospheric Chem. Phys., 4, 1461–1738, https://doi.org/10.5194/acp-4-1461-2004, 2004.

Bardouki, H., da Rosa, M. B., Mihalopoulos, N., Palm, W.-U., and Zetzsch, C.: Kinetics and mechanism of the oxidation of dimethylsulfoxide (DMSO) and methanesulfinate (MSI−) by OH radicals in aqueous medium, Atmos. Environ., 36, 4627–4634, https://doi.org/10.1016/S1352-2310(02)00460-0, 2002.

Barnes, I., Hjorth, J., and Mihalopoulos, N.: Dimethyl Sulfide and Dimethyl Sulfoxide and Their Oxidation in the Atmosphere, Chem. Rev., 106, 940–975, https://doi.org/10.1021/cr020529+, 2006.

657   Berndt, T., Scholz, W., Mentler, B., Fischer, L., Hoffmann, E. H., Tilgner, A., Hyttinen, N.,
658   Prisle, N. L., Hansel, A., and Herrmann, H.: Fast Peroxy Radical Isomerization and OH
659   Recycling in the Reaction of OH Radicals with Dimethyl Sulfide, J. Phys. Chem. Lett., 10,
660   6478–6483, https://doi.org/10.1021/acs.jpclett.9b02567, 2019.

661   Berndt, T., Hoffmann, E. H., Tilgner, A., Stratmann, F., and Herrmann, H.: Direct sulfuric acid
662   formation from the gas-phase oxidation of reduced-sulfur compounds, Nat. Commun., 14, 4849,
663   https://doi.org/10.1038/s41467-023-40586-2, 2023.

664   Bey, I., Jacob, D. J., Yantosca, R. M., Logan, J. A., Field, B. D., Fiore, A. M., Li, Q., Liu, H. Y.,
665   Mickley, L. J., and Schultz, M. G.: Global modeling of tropospheric chemistry with assimilated
666   meteorology: Model description and evaluation, J. Geophys. Res. Atmospheres, 106, 23073–
667   23095, https://doi.org/10.1029/2001JD000807, 2001.

668   Boniface, J., Shi, Q., Li, Y. Q., Cheung, J. L., Rattigan, O. V., Davidovits, P., Worsnop, D. R.,
669   Jayne, J. T., and Kolb, C. E.: Uptake of Gas-Phase SO2, H2S, and CO2 by Aqueous Solutions, J.
670   Phys. Chem. A, 104, 7502–7510, https://doi.org/10.1021/jp000479h, 2000.

671   Boucher, O., Moulin, C., Belviso, S., Aumont, O., Bopp, L., Cosme, E., von Kuhlmann, R.,
672   Lawrence, M. G., Pham, M., Reddy, M. S., Sciare, J., and Venkataraman, C.: DMS atmospheric
673   concentrations and sulphate aerosol indirect radiative forcing: a sensitivity study to the DMS
674   source representation and oxidation, Atmospheric Chem. Phys., 3, 49–65,
675   https://doi.org/10.5194/acp-3-49-2003, 2003.

676   Bräuer, P., Tilgner, A., Wolke, R., and Herrmann, H.: Mechanism development and modelling of
677   tropospheric multiphase halogen chemistry: The CAPRAM Halogen Module 2.0 (HM2), J.
678   Atmospheric Chem., 70, 19–52, https://doi.org/10.1007/s10874-013-9249-6, 2013.

679   Breider, T. J., Chipperfield, M. P., Richards, N. a. D., Carslaw, K. S., Mann, G. W., and
680   Spracklen, D. V.: Impact of BrO on dimethylsulfide in the remote marine boundary layer,
681   Geophys. Res. Lett., 37, https://doi.org/10.1029/2009GL040868, 2010.

682   Burkholder, J. B., Sander, S. P., Abbatt, J. P. D., Barker, J. R., Huie, R. E., Kolb, C. E., Kurylo,
683   M. J., Orkin, V. L., Wilmouth, D. M., and Wine, P. H.: Chemical kinetics and photochemical
684   data for use in atmospheric studies: evaluation number 18, 2015.

685   Burkholder, J. B., Sander, S. P., Abbatt, J. P. D., Barker, J. R., Cappa, C., Crounse, J. D., Dibble,
686   T. S., Huie, R. E., Kolb, C. E., Kurylo, M. J., Orkin, V. L., Percival, C. J., Wilmouth, D. M., and
687   Wine, P. H.: Chemical kinetics and photochemical data for use in atmospheric studies;
688   evaluation number 19, 2020.

689   Carslaw, K. S., Lee, L. A., Reddington, C. L., Pringle, K. J., Rap, A., Forster, P. M., Mann, G.
690   W., Spracklen, D. V., Woodhouse, M. T., Regayre, L. A., and Pierce, J. R.: Large contribution of
691   natural aerosols to uncertainty in indirect forcing, Nature, 503, 67–71,
692   https://doi.org/10.1038/nature12674, 2013.

693 Castebrunet, H., Martinerie, P., Genthon, C., and Cosme, E.: A three-dimensional model study of
694 methanesulphonic acid to non sea salt sulphate ratio at mid and high-southern latitudes,
695 Atmospheric Chem. Phys., 9, 9449–9469, https://doi.org/10.5194/acp-9-9449-2009, 2009.

696 Charlson, R. J., Lovelock, J. E., Andreae, M. O., and Warren, S. G.: Oceanic phytoplankton,
697 atmospheric sulphur, cloud albedo and climate, Nature, 326, 655–661,
698 https://doi.org/10.1038/326655a0, 1987.

699 Chen, H., Ezell, M. J., Arquero, K. D., Varner, M. E., Dawson, M. L., Gerber, R. B., and
700 Finlayson-Pitts, B. J.: New particle formation and growth from methanesulfonic acid,
701 trimethylamine and water, Phys. Chem. Chem. Phys., 17, 13699–13709,
702 https://doi.org/10.1039/C5CP00838G, 2015.

703 Chen, Q., Geng, L., Schmidt, J. A., Xie, Z., Kang, H., Dachs, J., Cole-Dai, J., Schauer, A. J.,
704 Camp, M. G., and Alexander, B.: Isotopic constraints on the role of hypohalous acids in sulfate
705 aerosol formation in the remote marine boundary layer, Atmospheric Chem. Phys., 16, 11433–
706 11450, https://doi.org/10.5194/acp-16-11433-2016, 2016.

707 Chen, Q., Schmidt, J. A., Shah, V., Jaeglé, L., Sherwen, T., and Alexander, B.: Sulfate
708 production by reactive bromine: Implications for the global sulfur and reactive bromine budgets,
709 Geophys. Res. Lett., 44, 7069–7078, https://doi.org/10.1002/2017GL073812, 2017.

710 Chen, Q., Sherwen, T., Evans, M., and Alexander, B.: DMS oxidation and sulfur aerosol
711 formation in the marine troposphere: a focus on reactive halogen and multiphase chemistry,
712 Atmospheric Chem. Phys., 18, 13617–13637, https://doi.org/10.5194/acp-18-13617-2018, 2018.

713 Chin, M., Jacob, D. J., Gardner, G. M., Foreman-Fowler, M. S., Spiro, P. A., and Savoie, D. L.:
714 A global three-dimensional model of tropospheric sulfate, J. Geophys. Res. Atmospheres, 101,
715 18667–18690, https://doi.org/10.1029/96JD01221, 1996.

716 Clarke, A. D., Davis, D., Kapustin, V. N., Eisele, F., Chen, G., Paluch, I., Lenschow, D., Bandy,
717 A. R., Thornton, D., Moore, K., Mauldin, L., Tanner, D., Litchy, M., Carroll, M. A., Collins, J.,
718 and Albercook, G.: Particle Nucleation in the Tropical Boundary Layer and Its Coupling to
719 Marine Sulfur Sources, Science, 282, 89–92, 1998a.

720 Clarke, A. D., Varner, J. L., Eisele, F., Mauldin, R. L., Tanner, D., and Litchy, M.: Particle
721 production in the remote marine atmosphere: Cloud outflow and subsidence during ACE 1, J.
722 Geophys. Res. Atmospheres, 103, 16397–16409, https://doi.org/10.1029/97JD02987, 1998b.

723 Du, L., Xu, Y., Ge, M., Jia, L., Yao, L., and Wang, W.: Rate constant of the gas phase reaction
724 of dimethyl sulfide (CH3SCH3) with ozone, Chem. Phys. Lett., 436, 36–40,
725 https://doi.org/10.1016/j.cplett.2007.01.025, 2007.

726 Duncan Fairlie, T., Jacob, D. J., and Park, R. J.: The impact of transpacific transport of mineral
727 dust in the United States, Atmos. Environ., 41, 1251–1266,
728 https://doi.org/10.1016/j.atmosenv.2006.09.048, 2007.

Emerson, E. W., Hodshire, A. L., DeBolt, H. M., Bilsback, K. R., Pierce, J. R., McMeeking, G. R., and Farmer, D. K.: Revisiting particle dry deposition and its role in radiative effect estimates, Proc. Natl. Acad. Sci., 117, 26076–26082, https://doi.org/10.1073/pnas.2014761117, 2020.

Enami, S., Nakano, Y., Hashimoto, S., Kawasaki, M., Aloisio, S., and Francisco, J. S.: Reactions of Cl Atoms with Dimethyl Sulfide: A Theoretical Calculation and an Experimental Study with Cavity Ring-Down Spectroscopy, J. Phys. Chem. A, 108, 7785–7789, https://doi.org/10.1021/jp049772y, 2004.

Faloona, I.: Sulfur processing in the marine atmospheric boundary layer: A review and critical assessment of modeling uncertainties, Atmos. Environ., 43, 2841–2854, https://doi.org/10.1016/j.atmosenv.2009.02.043, 2009.

Flyunt, R., Makogon, O., Schuchmann, M. N., Asmus, K.-D., and Sonntag, C. von: OH-Radical-induced oxidation of methanesulfinic acid. The reactions of the methanesulfonyl radical in the absence and presence of dioxygen, J. Chem. Soc. Perkin Trans. 2, 787–792, https://doi.org/10.1039/B009631H, 2001.

Fung, K. M., Heald, C. L., Kroll, J. H., Wang, S., Jo, D. S., Gettelman, A., Lu, Z., Liu, X., Zaveri, R. A., Apel, E. C., Blake, D. R., Jimenez, J.-L., Campuzano-Jost, P., Veres, P. R., Bates, T. S., Shilling, J. E., and Zawadowicz, M.: Exploring dimethyl sulfide (DMS) oxidation and implications for global aerosol radiative forcing, Atmospheric Chem. Phys., 22, 1549–1573, https://doi.org/10.5194/acp-22-1549-2022, 2022.

Galí, M., Levasseur, M., Devred, E., Simó, R., and Babin, M.: Sea-surface dimethylsulfide (DMS) concentration from satellite data at global and regional scales, Biogeosciences, 15, 3497–3519, https://doi.org/10.5194/bg-15-3497-2018, 2018.

Galí, M., Devred, E., Babin, M., and Levasseur, M.: Decadal increase in Arctic dimethylsulfide emission, Proc. Natl. Acad. Sci., 116, 19311–19317, https://doi.org/10.1073/pnas.1904378116, 2019.

Gershenzon, M., Davidovits, P., Jayne, J. T., Kolb, C. E., and Worsnop, D. R.: Simultaneous Uptake of DMS and Ozone on Water, J. Phys. Chem. A, 105, 7031–7036, https://doi.org/10.1021/jp010696y, 2001.

von Glasow, R. and Crutzen, P. J.: Model study of multiphase DMS oxidation with a focus on halogens, Atmospheric Chem. Phys., 4, 589–608, https://doi.org/10.5194/acp-4-589-2004, 2004.

Hezel, P. J., Alexander, B., Bitz, C. M., Steig, E. J., Holmes, C. D., Yang, X., and Sciare, J.: Modeled methanesulfonic acid (MSA) deposition in Antarctica and its relationship to sea ice, J. Geophys. Res. Atmospheres, 116, https://doi.org/10.1029/2011JD016383, 2011.

Hodshire, A. L., Campuzano-Jost, P., Kodros, J. K., Croft, B., Nault, B. A., Schroder, J. C., Jimenez, J. L., and Pierce, J. R.: The potential role of methanesulfonic acid (MSA) in aerosol formation and growth and the associated radiative forcings, Atmospheric Chem. Phys., 19, 3137–3160, https://doi.org/10.5194/acp-19-3137-2019, 2019.

Hoffmann, E. H., Tilgner, A., Schrödner, R., Bräuer, P., Wolke, R., and Herrmann, H.: An advanced modeling study on the impacts and atmospheric implications of multiphase dimethyl sulfide chemistry, Proc. Natl. Acad. Sci., 113, 11776–11781, https://doi.org/10.1073/pnas.1606320113, 2016.

Hoffmann, E. H., Heinold, B., Kubin, A., Tegen, I., and Herrmann, H.: The Importance of the Representation of DMS Oxidation in Global Chemistry-Climate Simulations, Geophys. Res. Lett., 48, e2021GL094068, https://doi.org/10.1029/2021GL094068, 2021.

Holmes, C. D., Bertram, T. H., Confer, K. L., Graham, K. A., Ronan, A. C., Wirks, C. K., and Shah, V.: The Role of Clouds in the Tropospheric NOx Cycle: A New Modeling Approach for Cloud Chemistry and Its Global Implications, Geophys. Res. Lett., 46, 4980–4990, https://doi.org/10.1029/2019GL081990, 2019.

Hoyle, C. R., Fuchs, C., Järvinen, E., Saathoff, H., Dias, A., El Haddad, I., Gysel, M., Coburn, S. C., Tröstl, J., Bernhammer, A.-K., Bianchi, F., Breitenlechner, M., Corbin, J. C., Craven, J., Donahue, N. M., Duplissy, J., Ehrhart, S., Frege, C., Gordon, H., Höppel, N., Heinritzi, M., Kristensen, T. B., Molteni, U., Nichman, L., Pinterich, T., Prévôt, A. S. H., Simon, M., Slowik, J. G., Steiner, G., Tomé, A., Vogel, A. L., Volkamer, R., Wagner, A. C., Wagner, R., Wexler, A. S., Williamson, C., Winkler, P. M., Yan, C., Amorim, A., Dommen, J., Curtius, J., Gallagher, M. W., Flagan, R. C., Hansel, A., Kirkby, J., Kulmala, M., Möhler, O., Stratmann, F., Worsnop, D. R., and Baltensperger, U.: Aqueous phase oxidation of sulphur dioxide by ozone in cloud droplets, Atmospheric Chem. Phys., 16, 1693–1712, https://doi.org/10.5194/acp-16-1693-2016, 2016.

Ishino, S., Hattori, S., Legrand, M., Chen, Q., Alexander, B., Shao, J., Huang, J., Jaeglé, L., Jourdain, B., Preunkert, S., Yamada, A., Yoshida, N., and Savarino, J.: Regional Characteristics of Atmospheric Sulfate Formation in East Antarctica Imprinted on 17O-Excess Signature, J. Geophys. Res. Atmospheres, 126, e2020JD033583, https://doi.org/10.1029/2020JD033583, 2021.

Jacob, D. J., Field, B. D., Li, Q., Blake, D. R., de Gouw, J., Warneke, C., Hansel, A., Wisthaler, A., Singh, H. B., and Guenther, A.: Global budget of methanol: Constraints from atmospheric observations, J. Geophys. Res. Atmospheres, 110, https://doi.org/10.1029/2004JD005172, 2005.

Jernigan, C. M., Fite, C. H., Vereecken, L., Berkelhammer, M. B., Rollins, A. W., Rickly, P. S., Novelli, A., Taraborrelli, D., Holmes, C. D., and Bertram, T. H.: Efficient Production of Carbonyl Sulfide in the Low-NOx Oxidation of Dimethyl Sulfide, Geophys. Res. Lett., 49, e2021GL096838, https://doi.org/10.1029/2021GL096838, 2022a.

Jernigan, C. M., Cappa, C. D., and Bertram, T. H.: Reactive Uptake of Hydroperoxymethyl Thioformate to Sodium Chloride and Sodium Iodide Aerosol Particles, J. Phys. Chem. A, 126, 4476–4481, https://doi.org/10.1021/acs.jpca.2c03222, 2022b.

Johnson, J. S. and Jen, C. N.: Role of Methanesulfonic Acid in Sulfuric Acid–Amine and Ammonia New Particle Formation, ACS Earth Space Chem., 7, 653–660, https://doi.org/10.1021/acsearthspacechem.3c00017, 2023.

Johnson, M. T.: A numerical scheme to calculate temperature and salinity dependent air-water transfer velocities for any gas, Ocean Sci., 6, 913–932, https://doi.org/10.5194/os-6-913-2010, 2010.

Kaufman, Y. J. and Tanré, D.: Effect of variations in super-saturation on the formation of cloud condensation nuclei, Nature, 369, 45–48, https://doi.org/10.1038/369045a0, 1994.

Khan, M. A. H., Gillespie, S. M. P., Razis, B., Xiao, P., Davies-Coleman, M. T., Percival, C. J., Derwent, R. G., Dyke, J. M., Ghosh, M. V., Lee, E. P. F., and Shallcross, D. E.: A modelling study of the atmospheric chemistry of DMS using the global model, STOCHEM-CRI, Atmos. Environ., 127, 69–79, https://doi.org/10.1016/j.atmosenv.2015.12.028, 2016.

Khan, M. A. H., Bannan, T. J., Holland, R., Shallcross, D. E., Archibald, A. T., Matthews, E., Back, A., Allan, J., Coe, H., Artaxo, P., and Percival, C. J.: Impacts of Hydroperoxymethyl Thioformate on the Global Marine Sulfur Budget, ACS Earth Space Chem., 5, 2577–2586, https://doi.org/10.1021/acsearthspacechem.1c00218, 2021.

Kloster, S., Feichter, J., Maier-Reimer, E., Six, K. D., Stier, P., and Wetzel, P.: DMS cycle in the marine ocean-atmosphere system – a global model study, Biogeosciences, 3, 29–51, https://doi.org/10.5194/bg-3-29-2006, 2006.

Kodros, J. K. and Pierce, J. R.: Important global and regional differences in aerosol cloud-albedo effect estimates between simulations with and without prognostic aerosol microphysics, J. Geophys. Res. Atmospheres, 122, 4003–4018, https://doi.org/10.1002/2016JD025886, 2017.

Kodros, J. K., Cucinotta, R., Ridley, D. A., Wiedinmyer, C., and Pierce, J. R.: The aerosol radiative effects of uncontrolled combustion of domestic waste, Atmospheric Chem. Phys., 16, 6771–6784, https://doi.org/10.5194/acp-16-6771-2016, 2016.

Kouvarakis, G. and Mihalopoulos, N.: Seasonal variation of dimethylsulfide in the gas phase and of methanesulfonate and non-sea-salt sulfate in the aerosols phase in the Eastern Mediterranean atmosphere, Atmos. Environ., 36, 929–938, https://doi.org/10.1016/S1352-2310(01)00511-8, 2002.

Kowalczuk, P., Cooper, W. J., Whitehead, R. F., Durako, M. J., and Sheldon, W.: Characterization of CDOM in an organic-rich river and surrounding coastal ocean in the South Atlantic Bight, Aquat. Sci., 65, 384–401, https://doi.org/10.1007/s00027-003-0678-1, 2003.

Kulmala, M.: How Particles Nucleate and Grow, Science, 302, 1000–1001, https://doi.org/10.1126/science.1090848, 2003.

Kulmala, M., Pirjola, L., and Mäkelä, J. M.: Stable sulphate clusters as a source of new atmospheric particles, Nature, 404, 66–69, https://doi.org/10.1038/35003550, 2000.

Lana, A., Bell, T. G., Simó, R., Vallina, S. M., Ballabrera-Poy, J., Kettle, A. J., Dachs, J., Bopp, L., Saltzman, E. S., Stefels, J., Johnson, J. E., and Liss, P. S.: An updated climatology of surface dimethlysulfide concentrations and emission fluxes in the global ocean, Glob. Biogeochem. Cycles, 25, https://doi.org/10.1029/2010GB003850, 2011.

Leaitch, W. R., Sharma, S., Huang, L., Toom-Sauntry, D., Chivulescu, A., Macdonald, A. M., von Salzen, K., Pierce, J. R., Bertram, A. K., Schroder, J. C., Shantz, N. C., Chang, R. Y.-W., and Norman, A.-L.: Dimethyl sulfide control of the clean summertime Arctic aerosol and cloud, Elem. Sci. Anthr., 1, 000017, https://doi.org/10.12952/journal.elementa.000017, 2013.

Lee, Y. H. and Adams, P. J.: A Fast and Efficient Version of the TwO-Moment Aerosol Sectional (TOMAS) Global Aerosol Microphysics Model, Aerosol Sci. Technol., 46, 678–689, https://doi.org/10.1080/02786826.2011.643259, 2012.

Lee, Y. H., Pierce, J. R., and Adams, P. J.: Representation of nucleation mode microphysics in a global aerosol model with sectional microphysics, Geosci. Model Dev., 6, 1221–1232, https://doi.org/10.5194/gmd-6-1221-2013, 2013.

Lennartz, S. T., Krysztofiak, G., Marandino, C. A., Sinnhuber, B.-M., Tegtmeier, S., Ziska, F., Hossaini, R., Krüger, K., Montzka, S. A., Atlas, E., Oram, D. E., Keber, T., Bönisch, H., and Quack, B.: Modelling marine emissions and atmospheric distributions of halocarbons and dimethyl sulfide: the influence of prescribed water concentration vs. prescribed emissions, Atmospheric Chem. Phys., 15, 11753–11772, https://doi.org/10.5194/acp-15-11753-2015, 2015.

Liu, H., Jacob, D. J., Bey, I., and Yantosca, R. M.: Constraints from 210Pb and 7Be on wet deposition and transport in a global three-dimensional chemical tracer model driven by assimilated meteorological fields, J. Geophys. Res. Atmospheres, 106, 12109–12128, https://doi.org/10.1029/2000JD900839, 2001.

Lucas, D. D. and Prinn, R. G.: Mechanistic studies of dimethylsulfide oxidation products using an observationally constrained model, J. Geophys. Res. Atmospheres, 107, ACH 12-1-ACH 12-26, https://doi.org/10.1029/2001JD000843, 2002.

Napari, I., Noppel, M., Vehkamäki, H., and Kulmala, M.: Parametrization of ternary nucleation rates for H2SO4-NH3-H2O vapors, J. Geophys. Res. Atmospheres, 107, AAC 6-1-AAC 6-6, https://doi.org/10.1029/2002JD002132, 2002.

Nightingale, P. D., Malin, G., Law, C. S., Watson, A. J., Liss, P. S., Liddicoat, M. I., Boutin, J., and Upstill-Goddard, R. C.: In situ evaluation of air-sea gas exchange parameterizations using novel conservative and volatile tracers, Glob. Biogeochem. Cycles, 14, 373–387, https://doi.org/10.1029/1999GB900091, 2000.

Novak, G. A., Fite, C. H., Holmes, C. D., Veres, P. R., Neuman, J. A., Faloona, I., Thornton, J. A., Wolfe, G. M., Vermeuel, M. P., Jernigan, C. M., Peischl, J., Ryerson, T. B., Thompson, C. R., Bourgeois, I., Warneke, C., Gkatzelis, G. I., Coggon, M. M., Sekimoto, K., Bui, T. P., Dean-Day, J., Diskin, G. S., DiGangi, J. P., Nowak, J. B., Moore, R. H., Wiggins, E. B., Winstead, E. L., Robinson, C., Thornhill, K. L., Sanchez, K. J., Hall, S. R., Ullmann, K., Dollner, M., Weinzierl, B., Blake, D. R., and Bertram, T. H.: Rapid cloud removal of dimethyl sulfide oxidation products limits SO2 and cloud condensation nuclei production in the marine atmosphere, Proc. Natl. Acad. Sci., 118, e2110472118, https://doi.org/10.1073/pnas.2110472118, 2021.

880 Novak, G. A., Kilgour, D. B., Jernigan, C. M., Vermeuel, M. P., and Bertram, T. H.: Oceanic
881 emissions of dimethyl sulfide and methanethiol and their contribution to sulfur dioxide
882 production in the marine atmosphere, Atmospheric Chem. Phys., 22, 6309–6325,
883 https://doi.org/10.5194/acp-22-6309-2022, 2022.

884 Park, R. J., Jacob, D. J., Field, B. D., Yantosca, R. M., and Chin, M.: Natural and transboundary
885 pollution influences on sulfate-nitrate-ammonium aerosols in the United States: Implications for
886 policy, J. Geophys. Res. Atmospheres, 109, https://doi.org/10.1029/2003JD004473, 2004.

887 Parrella, J. P., Jacob, D. J., Liang, Q., Zhang, Y., Mickley, L. J., Miller, B., Evans, M. J., Yang,
888 X., Pyle, J. A., Theys, N., and Van Roozendael, M.: Tropospheric bromine chemistry:
889 implications for present and pre-industrial ozone and mercury, Atmospheric Chem. Phys., 12,
890 6723–6740, https://doi.org/10.5194/acp-12-6723-2012, 2012.

891 Pham, M., Müller, J.-F., Brasseur, G. P., Granier, C., and Mégie, G.: A three-dimensional study
892 of the tropospheric sulfur cycle, J. Geophys. Res. Atmospheres, 100, 26061–26092,
893 https://doi.org/10.1029/95JD02095, 1995.

894 Pierce, J. R. and Adams, P. J.: Global evaluation of CCN formation by direct emission of sea salt
895 and growth of ultrafine sea salt, J. Geophys. Res. Atmospheres, 111,
896 https://doi.org/10.1029/2005JD006186, 2006.

897 Pound, R. J., Sherwen, T., Helmig, D., Carpenter, L. J., and Evans, M. J.: Influences of oceanic
898 ozone deposition on tropospheric photochemistry, Atmospheric Chem. Phys., 20, 4227–4239,
899 https://doi.org/10.5194/acp-20-4227-2020, 2020.

900 Pye, H. O. T., Liao, H., Wu, S., Mickley, L. J., Jacob, D. J., Henze, D. K., and Seinfeld, J. H.:
901 Effect of changes in climate and emissions on future sulfate-nitrate-ammonium aerosol levels in
902 the United States, J. Geophys. Res. Atmospheres, 114, https://doi.org/10.1029/2008JD010701,
903 2009.

904 Rosati, B., Isokääntä, S., Christiansen, S., Jensen, M. M., Moosakutty, S. P., Wollesen de Jonge,
905 R., Massling, A., Glasius, M., Elm, J., Virtanen, A., and Bilde, M.: Hygroscopicity and CCN
906 potential of DMS-derived aerosol particles, Atmospheric Chem. Phys., 22, 13449–13466,
907 https://doi.org/10.5194/acp-22-13449-2022, 2022.

908 Saunders, S. M., Jenkin, M. E., Derwent, R. G., and Pilling, M. J.: Protocol for the development
909 of the Master Chemical Mechanism, MCM v3 (Part A): tropospheric degradation of non-
910 aromatic volatile organic compounds, Atmospheric Chem. Phys., 3, 161–180,
911 https://doi.org/10.5194/acp-3-161-2003, 2003.

912 Schmidt, J. A., Jacob, D. J., Horowitz, H. M., Hu, L., Sherwen, T., Evans, M. J., Liang, Q.,
913 Suleiman, R. M., Oram, D. E., Le Breton, M., Percival, C. J., Wang, S., Dix, B., and Volkamer,
914 R.: Modeling the observed tropospheric BrO background: Importance of multiphase chemistry
915 and implications for ozone, OH, and mercury, J. Geophys. Res. Atmospheres, 121, 11,819-
916 11,835, https://doi.org/10.1002/2015JD024229, 2016.

917 Schobesberger, S., Junninen, H., Bianchi, F., Lönn, G., Ehn, M., Lehtipalo, K., Dommen, J.,
918 Ehrhart, S., Ortega, I. K., Franchin, A., Nieminen, T., Riccobono, F., Hutterli, M., Duplissy, J.,
919 Almeida, J., Amorim, A., Breitenlechner, M., Downard, A. J., Dunne, E. M., Flagan, R. C.,
920 Kajos, M., Keskinen, H., Kirkby, J., Kupc, A., Kürten, A., Kurtén, T., Laaksonen, A., Mathot, S.,
921 Onnela, A., Praplan, A. P., Rondo, L., Santos, F. D., Schallhart, S., Schnitzhofer, R., Sipilä, M.,
922 Tomé, A., Tsagkogeorgas, G., Vehkamäki, H., Wimmer, D., Baltensperger, U., Carslaw, K. S.,
923 Curtius, J., Hansel, A., Petäjä, T., Kulmala, M., Donahue, N. M., and Worsnop, D. R.: Molecular
924 understanding of atmospheric particle formation from sulfuric acid and large oxidized organic
925 molecules, Proc. Natl. Acad. Sci., 110, 17223–17228, https://doi.org/10.1073/pnas.1306973110,
926 2013.

927 Sehested, K. and Holcman, J.: A pulse radiolysis study of the OH radical induced autoxidation of
928 methanesulfinic acid, Radiat. Phys. Chem., 47, 357–360, https://doi.org/10.1016/0969-
929 806X(95)00115-E, 1996.

930 Sherwen, T., Schmidt, J. A., Evans, M. J., Carpenter, L. J., Großmann, K., Eastham, S. D., Jacob,
931 D. J., Dix, B., Koenig, T. K., Sinreich, R., Ortega, I., Volkamer, R., Saiz-Lopez, A., Prados-
932 Roman, C., Mahajan, A. S., and Ordóñez, C.: Global impacts of tropospheric halogens (Cl, Br, I)
933 on oxidants and composition in GEOS-Chem, Atmospheric Chem. Phys., 16, 12239–12271,
934 https://doi.org/10.5194/acp-16-12239-2016, 2016a.

935 Sherwen, T. M., Evans, M. J., Spracklen, D. V., Carpenter, L. J., Chance, R., Baker, A. R.,
936 Schmidt, J. A., and Breider, T. J.: Global modeling of tropospheric iodine aerosol, Geophys. Res.
937 Lett., 43, 10012–10019, https://doi.org/10.1002/2016GL070062, 2016b.

938 Sipilä, M., Berndt, T., Petäjä, T., Brus, D., Vanhanen, J., Stratmann, F., Patokoski, J., Mauldin,
939 R. L., Hyvärinen, A.-P., Lihavainen, H., and Kulmala, M.: The Role of Sulfuric Acid in
940 Atmospheric Nucleation, Science, 327, 1243–1246, https://doi.org/10.1126/science.1180315,
941 2010.

942 Spracklen, D. V., Pringle, K. J., Carslaw, K. S., Chipperfield, M. P., and Mann, G. W.: A global
943 off-line model of size-resolved aerosol microphysics: I. Model development and prediction of
944 aerosol properties, Atmospheric Chem. Phys., 5, 2227–2252, https://doi.org/10.5194/acp-5-2227-
945 2005, 2005.

946 Thomas, M. A., Suntharalingam, P., Pozzoli, L., Rast, S., Devasthale, A., Kloster, S., Feichter, J.,
947 and Lenton, T. M.: Quantification of DMS aerosol-cloud-climate interactions using the
948 ECHAM5-HAMMOZ model in a current climate scenario, Atmospheric Chem. Phys., 10, 7425–
949 7438, https://doi.org/10.5194/acp-10-7425-2010, 2010.

950 Trivitayanurak, W., Adams, P. J., Spracklen, D. V., and Carslaw, K. S.: Tropospheric aerosol
951 microphysics simulation with assimilated meteorology: model description and intermodel
952 comparison, Atmospheric Chem. Phys., 8, 3149–3168, https://doi.org/10.5194/acp-8-3149-2008,
953 2008.

954 Vehkamäki, H., Kulmala, M., Napari, I., Lehtinen, K. E. J., Timmreck, C., Noppel, M., and
955 Laaksonen, A.: An improved parameterization for sulfuric acid–water nucleation rates for

956 tropospheric and stratospheric conditions, J. Geophys. Res. Atmospheres, 107, AAC 3-1-AAC 3-
957 10, https://doi.org/10.1029/2002JD002184, 2002.

958 Veres, P. R., Neuman, J. A., Bertram, T. H., Assaf, E., Wolfe, G. M., Williamson, C. J.,
959 Weinzierl, B., Tilmes, S., Thompson, C. R., Thames, A. B., Schroder, J. C., Saiz-Lopez, A.,
960 Rollins, A. W., Roberts, J. M., Price, D., Peischl, J., Nault, B. A., Møller, K. H., Miller, D. O.,
961 Meinardi, S., Li, Q., Lamarque, J.-F., Kupc, A., Kjaergaard, H. G., Kinnison, D., Jimenez, J. L.,
962 Jernigan, C. M., Hornbrook, R. S., Hills, A., Dollner, M., Day, D. A., Cuevas, C. A.,
963 Campuzano-Jost, P., Burkholder, J., Bui, T. P., Brune, W. H., Brown, S. S., Brock, C. A.,
964 Bourgeois, I., Blake, D. R., Apel, E. C., and Ryerson, T. B.: Global airborne sampling reveals a
965 previously unobserved dimethyl sulfide oxidation mechanism in the marine atmosphere, Proc.
966 Natl. Acad. Sci., 117, 4505–4510, https://doi.org/10.1073/pnas.1919344117, 2020.

967 Vermeuel, M. P., Novak, G. A., Jernigan, C. M., and Bertram, T. H.: Diel Profile of
968 Hydroperoxymethyl Thioformate: Evidence for Surface Deposition and Multiphase Chemistry,
969 Environ. Sci. Technol., 54, 12521–12529, https://doi.org/10.1021/acs.est.0c04323, 2020.

970 Wang, W.-L., Song, G., Primeau, F., Saltzman, E. S., Bell, T. G., and Moore, J. K.: Global ocean
971 dimethyl sulfide climatology estimated from observations and an artificial neural network,
972 Biogeosciences, 17, 5335–5354, https://doi.org/10.5194/bg-17-5335-2020, 2020.

973 Wang, X., Jacob, D. J., Eastham, S. D., Sulprizio, M. P., Zhu, L., Chen, Q., Alexander, B.,
974 Sherwen, T., Evans, M. J., Lee, B. H., Haskins, J. D., Lopez-Hilfiker, F. D., Thornton, J. A.,
975 Huey, G. L., and Liao, H.: The role of chlorine in global tropospheric chemistry, Atmospheric
976 Chem. Phys., 19, 3981–4003, https://doi.org/10.5194/acp-19-3981-2019, 2019.

977 Wang, X., Jacob, D. J., Downs, W., Zhai, S., Zhu, L., Shah, V., Holmes, C. D., Sherwen, T.,
978 Alexander, B., Evans, M. J., Eastham, S. D., Neuman, J. A., Veres, P. R., Koenig, T. K.,
979 Volkamer, R., Huey, L. G., Bannan, T. J., Percival, C. J., Lee, B. H., and Thornton, J. A.: Global
980 tropospheric halogen (Cl, Br, I) chemistry and its impact on oxidants, Atmospheric Chem. Phys.,
981 21, 13973–13996, https://doi.org/10.5194/acp-21-13973-2021, 2021.

982 Wang, Y., Jacob, D. J., and Logan, J. A.: Global simulation of tropospheric O3-NO x -
983 hydrocarbon chemistry: 1. Model formulation, J. Geophys. Res. Atmospheres, 103, 10713–
984 10725, https://doi.org/10.1029/98JD00158, 1998.

985 Wesely, M. L.: Parameterization of surface resistances to gaseous dry deposition in regional-
986 scale numerical models, Atmospheric Environ. 1967, 23, 1293–1304,
987 https://doi.org/10.1016/0004-6981(89)90153-4, 1989.

988 Westervelt, D. M., Pierce, J. R., Riipinen, I., Trivitayanurak, W., Hamed, A., Kulmala, M.,
989 Laaksonen, A., Decesari, S., and Adams, P. J.: Formation and growth of nucleated particles into
990 cloud condensation nuclei: model–measurement comparison, Atmospheric Chem. Phys., 13,
991 7645–7663, https://doi.org/10.5194/acp-13-7645-2013, 2013.

992 Williamson, C. J., Kupc, A., Axisa, D., Bilsback, K. R., Bui, T., Campuzano-Jost, P., Dollner,
993 M., Froyd, K. D., Hodshire, A. L., Jimenez, J. L., Kodros, J. K., Luo, G., Murphy, D. M., Nault,
994 B. A., Ray, E. A., Weinzierl, B., Wilson, J. C., Yu, F., Yu, P., Pierce, J. R., and Brock, C. A.: A

995   large source of cloud condensation nuclei from new particle formation in the tropics, Nature,
996   574, 399–403, https://doi.org/10.1038/s41586-019-1638-9, 2019.

997   Wollesen de Jonge, R., Elm, J., Rosati, B., Christiansen, S., Hyttinen, N., Lüdemann, D., Bilde,
998   M., and Roldin, P.: Secondary aerosol formation from dimethyl sulfide – improved mechanistic
999   understanding based on smog chamber experiments and modelling, Atmospheric Chem. Phys.,
1000   21, 9955–9976, https://doi.org/10.5194/acp-21-9955-2021, 2021.

1001   Wu, R., Wang, S., and Wang, L.: New Mechanism for the Atmospheric Oxidation of Dimethyl
1002   Sulfide. The Importance of Intramolecular Hydrogen Shift in a CH3SCH2OO Radical, J. Phys.
1003   Chem. A, 119, 112–117, https://doi.org/10.1021/jp511616j, 2015.

1004   Zhang, J.-Z. and Millero, F. J.: The products from the oxidation of H2S in seawater, Geochim.
1005   Cosmochim. Acta, 57, 1705–1718, https://doi.org/10.1016/0016-7037(93)90108-9, 1993.

1006   Zhang, Y., Jacob, D. J., Maasakkers, J. D., Sulprizio, M. P., Sheng, J.-X., Gautam, R., and
1007   Worden, J.: Monitoring global tropospheric OH concentrations using satellite observations of
1008   atmospheric methane, Atmospheric Chem. Phys., 18, 15959–15973, https://doi.org/10.5194/acp-
1009   18-15959-2018, 2018.

1010   Zhou, Z.-X., Lujan, S. A., Burkholder, A. B., Garbacz, M. A., and Kunkel, T. A.: Roles for DNA
1011   polymerase δ in initiating and terminating leading strand DNA replication, Nat. Commun., 10,
1012   3992, https://doi.org/10.1038/s41467-019-11995-z, 2019.

1013   Zhu, L., Nicovich, J. M., and Wine, P. H.: Temperature-dependent kinetics studies of aqueous
1014   phase reactions of hydroxyl radicals with dimethylsulfoxide, dimethylsulfone, and
1015   methanesulfonate, Aquat. Sci., 65, 425–435, https://doi.org/10.1007/s00027-003-0673-6, 2003.

1016   Zhu, L., Nenes, A., Wine, P. H., and Nicovich, J. M.: Effects of aqueous organosulfur chemistry
1017   on particulate methanesulfonate to non–sea salt sulfate ratios in the marine atmosphere, J.
1018   Geophys. Res. Atmospheres, 111, https://doi.org/10.1029/2005JD006326, 2006.

1019   Zhu, L., Jacob, D. J., Eastham, S. D., Sulprizio, M. P., Wang, X., Sherwen, T., Evans, M. J.,
1020   Chen, Q., Alexander, B., Koenig, T. K., Volkamer, R., Huey, L. G., Le Breton, M., Bannan, T.
1021   J., and Percival, C. J.: Effect of sea salt aerosol on tropospheric bromine chemistry, Atmospheric
1022   Chem. Phys., 19, 6497–6507, https://doi.org/10.5194/acp-19-6497-2019, 2019.

1023